Zero-dimensional model of a reversible solid oxide fuel cell system with methanation

International Journal of Thermofluids 28 (2025) 101297

Contents lists available at ScienceDirect

International Journal of Thermofluids

journal homepage: www.sciencedirect.com/journal/international-journal-of-thermofluids

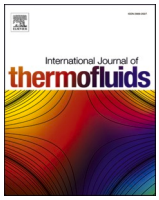

Zero-dimensional model of a reversible solid oxide fuel cell system with methanation

Zeinab Aghaziarati [a,b], Mohammad Ameri [a,*], Mokhtar Bidi [a], Paolo Marocco [b], Massimo Santarelli [b], Marta Gandiglio [b]

[a] Faculty of Mechanical and Energy Engineering, Shahid Beheshti University, Tehran, Iran
[b] Department of Energy, Politecnico di Torino, Torino, Italy

ARTICLE INFO

Keywords:
Reversible solid oxide fuel cell
Methane
Hydrogen
Electrolysis
Methanation

ABSTRACT

This paper investigates the use of Reversible Solid Oxide Cells (RSOCs) as a connection between electricity and gas networks. The system integrates an RSOC with a catalytic reactor for methane production via electrolysis and power generation in fuel cell mode. A 0-D computational model developed in Matlab, assesses its performance. In electrolysis mode, excess electricity is stored as hydrogen, which is then converted to methane for injection into gas infrastructure. In fuel cell mode, RSOC generates zero-emission electricity from methane or methane-hydrogen mixtures, as hydrogen is increasingly blended into natural gas grids. System's performance improves with higher hydrogen content, yielding 1.3–1.8 times more power and 11.8 % greater stack efficiency compared to pure methane. Fuel utilization, operating temperature, and steam-to-carbon ratio also impact performance. The roundtrip efficiency of the RSOC decreases with rising current density, dropping from 70.9 % to 28.6 %, with the overall system's roundtrip efficiency peaking at 0.14 A/cm^2.

1. Introduction

In recent years, energy has emerged as a significant global concern [1]. The energy grid's adoption of intermittent renewable sources poses several critical obstacles. For both storage and grid stability, an effective framework for energy conversion is required to manage the intermittent character of these renewable sources. Opting to store electrical energy as chemical energy offers distinct advantages, including greater storage capacity and enhanced facilitation within the sector [2]. Addressing these challenges, an RSOC reactor functions dually as an electrolyzer (SOEC) and a fuel cell (SOFC). During electrolysis mode, it stores electricity by producing synthetic fuel, while in its fuel cell mode, it generates electricity by electrochemically oxidizing fuel [3].

Several studies have concentrated on modeling stacks as RSOCs mostly with hydrogen or methane as fuels in the fuel cell mode, coupled with steam electrolysis or co-electrolysis. These studies also delve into the investigation of key parameters for enhanced performance. Kazempoor and Braun [4] introduced a model for an RSOC. They utilized activation and ohmic losses to verify the model, asserting that if these parameters closely match experimental data with reasonable precision, validation is successful. Additionally, they demonstrated that electrochemical losses differ significantly between each mode of operation. Mottaghizadeh et al. [5] modeled an RSOC and examined the impact of pressure on its performance. Their findings indicated that with increasing pressure from 1 bar to 25 bar, the stack efficiency rose from 56.3 % to 60.5 %. This increase in pressure also led to an elevation in Nernst voltage due to thermodynamic effects. Consequently, while higher pressure positively influenced the fuel cell, it had an adverse effect on the electrolysis process. Wendel et al. [6] discovered that augmenting the oxygen level of the oxidizer notably enhances both thermal and electrical effectiveness of the cell. However, they cautioned that challenges related to oxidant storage and parasitic load in the system may outweigh the advantages gained from this enhancement. Wendel et al. [7] discovered that the stack productivity is influenced by the fuel utilization factor. Nevertheless, they noted that this effect is insignificant, especially when assessed to variations in stack efficiency resulting from variations in current density. Hauck et al. [8] matured a simulation prototype of an RSOC using Aspen Plus and examined the influence of inlet gas mixture, pressure, and temperature. They found that changes in hydrogen and steam concentrations affected RSOFC performance, with increased hydrogen enhancing the fuel cell mode but impairing electrolysis, and vice versa for steam. Increasing operating temperature improved RSOFC performance overall, and pressurized

* Corresponding author.
E-mail address: m_ameri@sbu.ac.ir (M. Ameri).

https://doi.org/10.1016/j.ijft.2025.101297

Available online 10 June 2025

Nomenclature

Symbols

A	Area (cm^2)
c_p	Specific heat capacity ($J/kg.K$)
D	Molecular diffusion
d_p	Mean pore size (m)
F	Faraday constant (C/mol)
h	Specific enthalpy (J/kg)
ΔH_{rxn}	Standard enthalpy of formation (J/mol)
i	Current density (A/cm^2)
I	Current (A)
k_B	Boltzmann's constant
LHV	Lower heating value (J/kg)
$\dot{m}$	Mass flow rate (kg/s)
M	Molar weight (kg/mol)
$\dot{N}$	Molar flow rate (mol/s)
P	Pressure (KPa)
Q	Heat rate (W)
r	Recirculation rate
R	Universal gas constant ($J/mol.K$)
SC	Steam conversion ratio
T	Temperature (K)
U_f	Fuel utilization factor
V	Voltage (V)
W	Power density (W)
y	Molar fraction

Abbreviations

ASR	Area specific resistance
BoP	Balance of plant
RSOC	Reversible solid oxide cell
SMR	Steam reforming of methane
SOEC	Solid oxide electrolysis cell
SOFC	Solid oxide fuel cell
TPB	Three phase boundaries
WGS	Water-gas shift

Greek letters

ξ	Molar extent (mol/s)
λ	Air ratio
η	Efficiency
γ	Heat capacity ratio
ν	Specific volume (m^3/kg)
μ	Steam-to-carbon ratio
δ	Thickness (cm)
σ	Conductivity (S/cm)
$\sigma_{i,j}$	Mean characteristic length of species i and j
ϕ	Frequency factor (A/m^2)
ξ	Tortuosity
θ	Porosity
Ω_D	Diffusion collision integral
Γ	Dimensionless temperature coefficient
$\varepsilon_{i,j}$	Lennard-Jones energy

Subscripts

c	Cold stream
EL	Electrolysis
el	Electrical
FC	Fuel cell
h	Hot stream
in	Inlet
is	Isentropic
mech	Mechanical
op	Operating
out	Outlet
r	Reversible
stoich	Stoichiometric
t	Time
tot	Total

Acronyms

A	Air
F	Feed
P	Product

operation enhanced fuel cell mode performance by increasing operational voltage and reducing diffusion losses. Botta et al. [9] investigated the dynamic activity of an RSOC, finding that the cell's productivity is significantly influenced by the temperature of solid-state and operational current density. Optimal operational parameters, like temperature, and current density affect irreversible depletions and cell voltage. Santhanam et al. [10] studied RSOC parameters theoretically and in an ideal state (without losses). They also conducted an experimental investigation on a commercial RSOC. Results showed that a roundtrip efficiency of 55–60 % can be achieved. They also introduced the storing of thermal energy as a suitable way to manage the two modes, since the required heat for electrolyzer mode is <10 % of the produced heat in the fuel cell mode.

Numerous investigations have centered around the modeling and analysis of SOFCs. Colpan et al. [11] modeled a direct internal reforming SOFC. Their findings revealed that augmenting the recirculation ratio reduces output power and consequently stack efficiency at higher current densities. Moreover, they emphasized the critical role of fuel utilization factor, showing that high ratios lead to lower power generation and air consumption rate but higher efficiency. Ni et al. [12] developed a model for SOFCs and found ideal values for porosity and pore size of electrode to maximize cell productivity. While activation and ohmic losses diminished with rising temperature, the concentration losses unexpectedly increased because of reduced gas density at higher temperatures. They also identified increasing hydrogen percentage in the fuel flow compared to steam and raising operating pressure as effective methods for enhancing SOFC power output. Chan et al. [13] conducted an analysis on a SOFC with external reformer fueled by hydrogen and methane. They found that under specific conditions, an H_2-fed system achieved an efficiency of 50.97 %. In contrast, under the same conditions, a CH_4-fed system yielded a higher efficiency of 62.19 %. Monforti Ferrario et al. [14] evaluated an anode supported SOFC with external reforming. They used three gas compositions including 100 % H_2, 67 % H_2+33 % natural gas, and 100 % natural gas as inlet fuel. Their test findings showed that the peak voltage and power is gained in the 100 % H_2 case, however from efficiency standpoint, utilizing 100 % natural gas is preferable. The reason is that external reformation produces a fuel which has diminished energy level. Mojaver et al. [15] conducted a comparative analysis of SOFCs using oxygen ion- conducting and proton-conducting electrolytes, concluding that the oxygen ion-conducting type performs better in terms of energy, exergy, economic, and environmental criteria across the tested conditions. Singh and Bhogilla [16] found that increasing current density in SOFCs lowers exergy efficiency due to reduced voltage and higher exergy destruction. They also showed that raising the operating temperature improves exergy efficiency up to 900 K. However, beyond this point, exergy efficiency drops because the excess heat generated at higher temperatures leads to greater exergy losses in the system.

A few research endeavors have concentrated on the integration of RSOC with methanation reactors. Chen et al. [17] developed a 2D model

of a pressurized RSOC coupled with methanation and showed that elevated pressure significantly enhances methane production by boosting both electrochemical and chemical reaction rates. Their study highlighted the interplay between methanation and electrolysis, especially under SOEC mode. Bin et al. [18] proposed a MW-scale integrated system combining RSOC with CO_2 methanation for dynamic grid electricity storage. Their model demonstrated high power-to-gas efficiency (up to 85 %) and effective methane production under various operating modes. A control strategy was developed to manage H_2 storage and optimize system flexibility under fluctuating grid conditions. Methane stands out as a predominant hydrocarbon and a crucial medium for electricity production. Utilizing methanation reactors represents the predominant methodology within power-to-gas frameworks owing to their notable conversion efficiency, ranging between 49 % to 65 % [19]. Wang et al. [20] explored a power-to-methane system and found that the operational point of the SOEC, specifically the steam utilization factor, dictates the reliance on internal heat sources for steam generation. In their analyzed system, with steam utilization exceeding 60 %, all steam production can be achieved without electrical heating, primarily fueled by methanation heat (80–85 %) supplemented by heat from the anode outlet (15–18 %). Foit et al. [21] proposed power-to-methane through SOEC, highlighting its elevated electrical efficiency and cost competitiveness relative to other power-to-methane approaches. The findings from Luo's investigation into SOEC combined with methanation demonstrated a system efficiency of 76 %. This superior efficiency was attributed to the integration of methanation for steam generation within the SOEC, outperforming conventional low-temperature electrolysis systems by 15–25 % [22]. Zhong et al. [23] examined the essential operational factors of a solar-powered power-to-methane system that integrates SOEC with a methanation reactor. Their results indicated that optimizing the synthetic natural gas yield involves reducing the utilization factor and operating pressure of the SOEC, while increasing the air-water ratio and inlet temperature of it.

Some studies have proposed various techniques for storing the waste heat generated by RSOC to enhance the overall system efficiency. These methods include utilizing metal hydrides [24], phase change materials [5], or thermochemical energy storage [25]. Additionally, some research efforts have concentrated on integrating RSOC with other cycles to develop multi-generation systems [26–35]. Mojaver et al. [36] modeled a co-generation system combining SOFC, supercritical carbon dioxide Brayton cycle, ORC, and heat recovery using a zero-dimensional approach. They analyzed the effects of current density, fuel utilization, and anode recycle ratio on system performance. Results showed current density had the greatest impact.

Through a comprehensive literature review, it is evident that the majority of research papers focus on modeling i-V curves of stacks, validating results, devising control strategies, or investigating compositions of hydrogen and steam as inlet flow. However, there is a notable scarcity of studies investigating complete systems encompassing both RSOC and Balance of Plant (BoP) elements. Furthermore, there is a significant research gap concerning the combination of methanation with RSOC, exploration of different hydrogen and methane compositions as inlet flows in fuel cell mode, and examination of the steam-to-carbon ratio's impact on system operation. This study addresses these gaps by extending a system developed in [37], which is based on RSOC technology and coupled with a methanation unit to generate methane in electrolysis mode and produce green energy in fuel cell mode. The system can provide grid flexibility by storing excess power in the form of hydrogen when operating in electrolyzer mode. Hydrogen is then converted to methane for easy injection into existing gas infrastructure, a process that is also explored in this study. In fuel cell mode, the system generates high-efficiency, zero-emissions electricity, running on pure methane or a mixture of hydrogen and methane. Given the increasing likelihood of hydrogen blending in natural gas grids, it is important to understand the performance of SOFCs under varying fuel compositions, especially as the transition to a full hydrogen infrastructure progress. While variations in fuel composition, such as the inclusion of carbon monoxide (CO) or other hydrocarbons, are relevant to combustion systems in broader applications, these considerations are beyond the scope of the present work. A detailed 0-D computational model is developed using Matlab® to investigate stack functioning parameters and BoP elements in both modes. The analysis is strengthened by a detailed electrochemical model of the RSOC - covering both fuel cell and electrolysis operation - to account for performance variations under changing operating conditions. This model is also validated using experimental data under variable operating mixture conditions. Additionally, the study examines the impact of inlet flow composition on fuel cell operation by varying methane and hydrogen percentages. It also explores the influence of critical parameters such as fuel utilization factor, steam-to-carbon ratio, and operating temperature.

2. System description

This segment outlines the configuration of the examined arrangement, capable of functioning in fuel cell and electrolysis modes. When operating in fuel cell mode, the RSOC initiates inside reformation of the incoming fuel in the presence of water to generate the necessary hydrogen for the electrochemical process. To facilitate methane reforming and prevent carbon residue on the electrode interface, an anode gas recycling flow is utilized. In electrolysis mode, the RSOC utilizes electrical input to drive a reaction that is thermodynamically unfavorable.

2.1. Fuel cell mode

A diagram illustrating the proposed system operating in fuel cell mode is depicted in Fig. 1-a. Following the fuel compressor pressurizing the inlet fuel (F2), it merges with the recirculated gas mixture (P2) before entering the fuel pre-heater (F3). The mixture's temperature rises within the fuel pre-heater (F4) before entering the anode channel. Simultaneously, the inlet air undergoes pressurization via an air blower (A2) and is heated in the air pre-heater (A5) prior to entering the cathode channel. At the anode, methane steam reforming, water-gas shift, and electrochemical reactions occur concurrently. O_2 from the air undergo a reaction with electrons generated at the anode and then circulate. This flow of electrons generates electric current, which performs work on the load. Due to the elevated water level in the fuel duct exit stream (P1), a portion is recirculated (P2) since water is essential for methane reforming. The exhaust streams from the stack (P3 and A6) enter the catalytic combustor, where unreacted fuel undergoes combustion, converting chemical energy into thermal energy. To regulate the combustor's temperature within permissible limits, an air bypass stream (A4) supplies cold air. The resulting high-temperature outlet stream from the combustor (P4) preheats incoming fuel and air upon passing through fuel and air preheaters (P5 and P6).

2.2. Electrolysis and methanation mode

The process layout for electrolysis mode is illustrated in Fig. 1-b. A water pump elevates the inlet water pressure (F2), after which the water proceeds through a heat exchanger. Subsequently, upon temperature elevation (F3), it enters evaporator to transform into steam (F4). In instances where the requisite energy for water vaporization is lacking, a feed electrical heater is utilized (F5). Analogous to fuel cell operation mode, subsequent to steam pressure elevation via a blower (F6), it combines with recirculated gas (P2) and enters the pre-heater (F7). Post pre-heater (F8) passage, the mixture's temperature rises before entering the fuel duct. Sweep air is pressurized by the air blower (A2) as well, heated in an air heat exchanger (A3), and then enters the air channel.

Within the stack, chemical reactions occur, and the recirculation of outlet flow (P2) facilitates a little H_2 portion influx to the inlet flow, preventing Ni electrode oxidation. The residual fuel electrode outlet

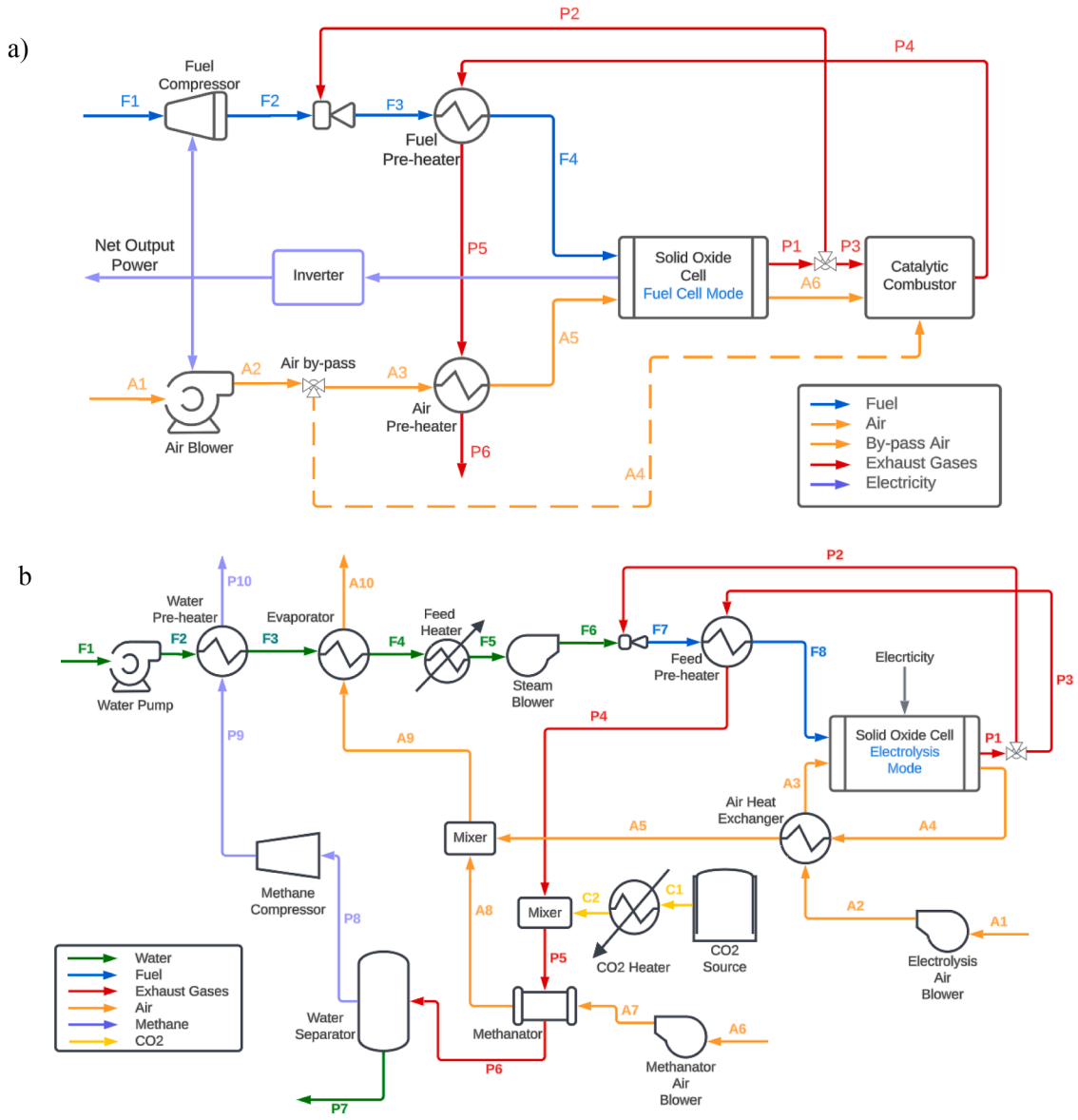

Fig. 1. Layout of the framework in fuel cell (a) and electrolysis (b) modes operation, modified from [37].

stream (P3) enters a pre-heater to furnish the necessary energy for inlet stream pre-heating. Downstream CO_2 is heated in an electrical heater to reach methanation temperature (C2). Cathode outlet stream and CO_2 converge (P5) and enter the methanation unit, where required air for managing methanation reaction enters the unit post-pressure increase via a blower (A7). As separation is required for water produced in methanation process, a water separator is employed. Methanation unit outlet stream (P6) enters the water separator, where condensed water removed from the flash tank (P7) in flash pressure (P_{flash}) and temperature (T_{flash}). Subsequently, produced methane (P8) undergoes compression to reach injection network pressure (P10). As the outlet methane stream temperature post-compression is high, it is utilized to heat the electrolyzer inlet water, increasing its temperature.

Post-air channel exhaust (A4), subsequent to passing through a heat exchanger and elevating incoming air temperature (A5), mixes with methanation unit exhaust air (A8) before supplying the evaporator's prime energy. During endothermic electrolysis operation, where sweep air is unnecessary, only the oxygen produced during the electrolysis process passes through the heat exchanger (A4).

3. System modelling

A 0-D model is crafted using Matlab® to delve into the electrochemical and thermodynamic intricacies within the reversible solid oxide cell, as well as to analyze the thermodynamic processes of various components within the system. Ambient pressure and temperature are fixed at 100 kPa and 298 K, respectively, in the modeling.

3.1. Reversible solid oxide cell

The provided model for the RSOC contains of electrochemical modeling along with mass and energy equations. The required input parameters for modeling are presented in Table 1. The model is formulated under the subsequent presumptions [11]:

- The solid oxide cell functions under steady-state conditions and it operates adiabatically.
- The electrochemical reactions involving CO and CO_2 are disregarded.
- Both fuel and air enter the cell with the uniform temperature (T_{in}). Similarly, exhaust gases and air exit the cell with the equal

Table 1
Input data.

Parameter	Unit	Value			Ref.
		Both modes	Electrolysis mode	Fuel cell mode	
Total active area (A_{tot})	m^2	5			
Operating pressure (P_{cell})	kPa	100			
Operating temperature (T_{op})	K	1073			
Temperature difference (ΔT_{cell})	K	100			
Universal gas constant (R)	J/(mol•K)	8.3145			
Faraday constant (F)	C/mol	9.65e4			
Fuel utilization factor (U_f)	–		–	0.8	
Steam-to-carbon ratio (μ)			–	2.5	
Recirculation rate (r_{EL})	–		0.1		
Steam conversion ratio (SC)	–		0.9	–	
Inlet fuel composition	%mol.		100 % H_2O	100 % CH_4	
Inlet air composition	%mol.		79 % N_2+21 %O_2	79 % N_2+21 % O_2	
Pump/ blower isentropic efficiency ($\eta_{is,pump/blower}$)	%	80			[40]
Compressor mechanical efficiency ($\eta_{mech,comp}$)	%	90			[41]
Compressor isentropic efficiency ($\eta_{is,comp}$)	%	80			[40]
Inverter efficiency ($\eta_{inverter}$)	%	98			[42]
Electrical efficiency of heater/ cooler (η_{el})	%	95			[43]
Pressure of injection (P_{P10})	MPa	3			[44]
Temperature of injection (T_{P10})	K	323			[45]
Temperature rises in methanation ($\Delta T_{methanation}$)	K	100			[46]
Inlet temperature of methanation reactor (T_{P5},T_{A7})	K	523			[46]
Flash pressure (P_{flash})	kPa	100			[47]
Flash temperature (T_{flash})	K	303			[47]
Pressure drops of pre-heater	kPa	10			[48]
Pressure drops of RSOC	kPa	3			[49]
Pressure drops of evaporator	kPa	1			[50]
Pressure drops of methanation unit	kPa	15			[51]
Pressure drops of combustor	kPa	2			[48]
Tortuosity (ξ)	–	5.4			[12]
Porosity (θ)	–	0.48			[12]
frequency factor of fuel electrode ($\phi_{fuelelectrode}$)	A/m^2	1.9×10^{10}			[52]
frequency factor of air electrode ($\phi_{airelectrode}$)	A/m^2	1.4×10^{9}			[52]
Fuel electrode activation energy ($E_{activation,fuelelectrode}$)	kJ/mol	100			[12]
Air electrode activation energy ($E_{activation,airelectrode}$)	kJ/mol	120			[12]
electrolyte activation energy ($E_{activation,electrolyte}$)	kJ/mol	10.3			[12]
Mean pore size (d_p)	μm	1			[12]
Fuel electrode thickness ($\delta_{fuelelectrode}$)	μm	750			[12]
Air electrode thickness ($\delta_{airelectrode}$)	μm	50			[12]
Electrolyte thickness ($\delta_{electrolyte}$)	μm	50			[12]
Specific conductivity of fuel electrode ($\sigma_{0,fuelelectrode}$)	S•K/m	8.11×10^{-5}			[53]
Specific conductivity of air electrode ($\sigma_{0,airelectrode}$)	S•K/m	2.98×10^{-5}			[53]
Specific conductivity of electrolyte ($\sigma_{0,electrolyte}$)	S•K/m	2.94×10^{-5}			[53]

temperature (T_{out}). The cell temperature (T_{op}) is presumed to be the mean value of the inlet (T_{in}) and outlet temperature (T_{out}) of flows.
- Single cell performance is utilized to represent the entire RSOC stack [38,39].
- Each reaction is regarded as being in a state of equilibrium.
- Pressure drop across the cell is disregarded for cell-level calculations.

3.1.1. Mass balances for fuel cell operation

The concurrent process at the fuel electrode involves the methane steam reforming reaction, water–gas shift reaction and hydrogen oxidation, which are presented in Eqs. (1)–(3), respectively.

$$CH_4 + H_2O \leftrightarrow CO + 3H_2 \quad (1)$$

$$CO + H_2O \leftrightarrow H_2 + CO_2 \quad (2)$$

$$H_2 + \frac{1}{2}O_2 \rightarrow H_2O \quad (3)$$

Computing the molar flow rate of species j in stream i ($\dot{N}_i^j$), involves multiplying its molar fraction (y_i^j) by the overall molar flow rate of the stream ($\dot{N}_i$) according to Eq. (4).

$$\dot{N}_i^j = \sum y_i^j \cdot \dot{N}_i \quad (4)$$

The equations for calculating the molar flow rates of different flows are provided in Appendix A in detail, following the approach from [37]. The steam-to-carbon ratio (μ) which indicates the amount of steam relative to carbon in the fuel mixture is defined in Eq. (5).

$$\mu = \dot{N}_{F4}^{H_2O} / \dot{N}_{F4}^{C} \quad (5)$$

In the context of oxygen electrode modeling, the molar flow rate of air entering it comprises two components: the stoichiometric value of air necessary for the reaction ($\dot{N}_{Stoich}^{Air}$) and the additional air necessary to uphold the temperature difference of the cell lesser ΔT_{cell} ($\dot{N}_{Sweep}^{Air}$). The

use of sweep air plays a critical role in thermal management by removing excess heat generated during RSOC operation. This strategy helps regulate the temperature profile across the cell stack, preventing excessive thermal gradients that could lead to mechanical stress, material degradation, or reduced efficiency. The amount of sweep air is carefully controlled based on the desired cell temperature and heat load, ensuring the cell remains within its safe operational window. The components are calculated using Eqs. (6) and 7 [11]:

$$\dot{N}^{Air}_{Stoich} = \frac{\xi_{redox}}{2} + \frac{\xi_{redox}}{2}\cdot\frac{79}{21} \tag{6}$$

$$\dot{N}^{Air}_{Sweep} = \frac{Q_{Stack,FC}/M_A}{h_{A6} - h_{A5}} \tag{7}$$

where $Q_{Stack,FC}$ represents the generated heat by the stack, M_A is the molar weight of air, and h denotes the specific enthalpy. The air ratio (λ_A) is ultimately specified as follow:

$$\lambda_A = \frac{\dot{N}^{Air}_{Stoich} + \dot{N}^{Air}_{Sweep}}{\dot{N}^{Air}_{Stoich}} \tag{8}$$

3.1.2. Electrochemical model for fuel cell operation

The generated power by the stack (W_{op}) can be calculated using an electrochemical relationship [54].

$$W_{op} = V_{op}.I_{cell} \tag{9}$$

where V_{op} and I_{cell} are operating voltage and current of the stack, respectively. They can be calculated from the following relations [39, 55]:

$$V_{op} = V_r - V_{loss} \tag{10}$$

$$I_{cell} = i_{op}\cdot A_{tot} \tag{11}$$

The value of current density (i_{op}) and surface area (A_{tot}) of the stack are provided in Table 1. V_r and V_{loss} represent the reversible and loss voltages, defined in Eqs. (12) and 14.

$$V_r = E^0_r + \frac{RT_{op}}{2F}\ln\left[\frac{y^{H2}_{P1}\sqrt{y^{O2}_{P1}}}{y^{H2O}_{P1}}\right] \tag{12}$$

E^0_r is equilibrium potential which can be calculated by Eq. (13) [56]. R and F stand respectively for universal gas constant and Faraday constant. The term y^j_{P1} signifies the equilibrium molar fraction of j-th specie of the outlet flow of the stack.

$$E^0_r = 1.26485 - 2.4725\cdot10^{-4}T_{op} - 1.875\cdot10^{-8}{T_{op}}^2 \tag{13}$$

$$V_{loss} = V_{ohmic} + V_{activation} + V_{concentration} \tag{14}$$

The detailed equations for calculating the various overpotentials are provided in Appendix B, while the characteristics of the stack are presented in Table 1.

3.1.3. Energy balance for fuel cell operation

The produced heat by the stack ($Q_{stack,FC}$), which should be eliminated by the purge gas is determined by conducting an energy balance for the stack.

$$Q_{stack,FC} = \sum \dot{m}^j_{P1}\cdot h^j_{P1} - \sum \dot{m}^j_{F4}\cdot h^j_{F4} + W_{op} + \xi_{SMR}\cdot\Delta H_{rxn\_MR} + \xi_{WGS}\cdot\Delta H_{rxn\_WGS} + \xi_{redox}\cdot\Delta H_{rxn\_redox} \tag{15}$$

Where $\dot{m}$ is mass flow rate. ΔH_{rxn_MR}, ΔH_{rxn_WGS}, and ΔH_{rxn_redox} represent the heat of reactions 1, 2, and 3, respectively. W_{op} is generated power by stack which is calculated according to Eq. (9). The stack's efficiency ($\eta_{stack,FC}$) is characterized by dividing the gross power produced by the stack (excluding BoP energy demands) by the total energy of the feed (established using the LHV). LHV^j_{F2} is lower heating value of species j of inlet fuel [55].

$$\eta_{stack,FC} = \frac{W_{op},FC}{\sum \dot{m}^j_{F4}\cdot LHV^j_{F4}} \tag{16}$$

3.1.4. Mass balance for electrolysis mode

Since only water electrolysis is taken into account during electrolysis mode, the mass balance is significantly simplified. The electrochemical reaction in this mode is expressed as:

$$H_2O \rightarrow H_2 + \frac{1}{2}O_2 \tag{17}$$

when given the operating current density (i_{op}), Faraday's law allows the calculation of the molar extent of the electrochemical reaction (ξ_{EL}) according to Eq. (18) [57].

$$\xi_{EL} = \frac{i_{op}}{2F}\cdot A_{tot} \tag{18}$$

The detailed equations for calculating the molar flow rates of various flows can be found in Appendix A. In electrolysis mode, the O_2 electrode balance differs with fuel cell mode because oxygen is not a reactant for the stack. Although blowing air into the oxygen electrode is not required, it is common to flow air through it to regulate the operating temperature, especially when the cell is exothermic. This helps maintain a consistent average temperature and manage thermal stress. Air can be swept through the oxygen electrode duct to control the temperature gradient, similar to fuel cell mode. The molar flow rates of air are determined to manage these conditions.

$$\dot{N}_{A3} = \dot{N}^{Air}_{Sweep} \tag{19}$$

$$\dot{N}_{A4} = \dot{N}^{O_2}_{Stoich} + \dot{N}^{Air}_{Sweep} \tag{20}$$

The molar flow rate of sweep air ($\dot{N}^{Air}_{Sweep}$) is computed using Eq. (7). $\dot{N}^{O_2}_{Stoich}$ represents the stoichiometrically generated O_2 during electrolysis, which is equal to $\xi_{EL}/2$.

3.1.5. Electrochemical model for electrolysis mode

The electrochemical model developed for fuel cell is applicable to electrolysis as well. Hence, Eqs. (9)–(12) hold valid. To determine the equilibrium potential (E^0_r) in electrolysis mode, the following relationship can be utilized [58]:

$$E^0_r = 1.253 - 0.0024516\cdot T_{op} \tag{21}$$

Since SOFC and SOEC represent various functional states of an RSOC, the stack properties outlined in Table 1 and the loss calculation procedures remain consistent across both modes.

3.1.6. Energy balance for electrolysis mode

By conducting an energy balance around the stack, the generated or produced heat of the stack can be calculated:

$$Q_{Stack,EL} = -\sum \dot{m}^j_{P1}\cdot h^j_{P1} + \sum \dot{m}^j_{F8}\cdot h^j_{F8} - W_{op,EL} - \xi_{EL}\cdot\Delta H_{H_2} \tag{22}$$

The required power for the stack in electrolysis mode ($W_{op,EL}$) can be determined using Eq. (9). ΔH_{H_2} denotes the enthalpy change for the oxidation of H_2, as per Eq. (17).

In electrolysis mode, the stack's efficiency is denoted as the ratio of total energy of the exiting H_2 to the gross power used by the stack, neglecting BoP energy requirements [55].

$$\eta_{stack,EL} = \frac{\xi_{EL}\cdot LHV_{H_2}}{W_{op,EL}} \tag{23}$$

3.2. Balance of plant

The balance of plant components involves all units essential for compression, heating, cooling, mixing, and reaction, situated outside the stack. These elements are modeled as control volumes employing thermodynamic equations and writing first law of thermodynamic for each component. The detailed modeling of the system components is provided in Appendix C [37], while the input parameters for BoP modeling are outlined in Table 1.

3.2.1. System efficiency

System efficiency for each mode of operation defined in Eq. (24) which is influenced by parasitic power consumption of ancillary equipment, is. system parasitic is calculated for both modes in Eq. (25).

$$\eta_{system} = \begin{cases} \dfrac{W_{op,FC} - W_{parasitic}}{\sum \dot{m}^{j}_{F1} \cdot LHV^{j}_{F1}} & \text{fuel cell mode} \\ \dfrac{\dot{m}_{P9} \cdot LHV_{CH4}}{W_{op,EL} + W_{parasitic}} & \text{electrolysis mode} \end{cases} \tag{24}$$

$$W_{parasitic} = \begin{cases} W_{blower} + W_{compressor} + W_{inverter} & \textit{fuel cell mode} \\ \sum W_{blower} + W_{compressor} + W_{pump} + \sum W_{el,heater} + W_{inverter} & \textit{electrolysis mode} \end{cases} \tag{25}$$

The roundtrip efficiency for RSOC ($\eta_{RT,RSOC}$) and overall system ($\eta_{RT,system}$) are defined in Eqs. (26) and (27), respectively, as function of operating duration (t_{op}) in SOFC and SOEC modes [5,59].

$$\eta_{RT,\ RSOC} = \frac{W_{op,FC} \cdot t_{op,FC}}{W_{op,EL} \cdot t_{op,EL}} \tag{26}$$

$$\eta_{RT,\ system} = \frac{W_{op,FC} \cdot t_{op,FC} - W_{parasitic}}{W_{op,EL} \cdot t_{op,EL} + W_{parasitic}} \tag{27}$$

4. Validation

To validate the proposed modeling approach, experimental data from [60] and [61] are used to verify the RSOC model. The comparison of Cases I to III is presented in Fig. 2-a, which corresponds to the RSOC operating with hydrogen fuel. Cases IV and V are presented in Fig. 2-b, related to the fuel cell feed with methane and a combination of hydrogen and methane. Case I and Case II operate in both fuel cell and electrolysis modes. Case III operates solely in electrolysis mode and cases IV and V operate only in fuel cell mode. All input parameters are as listed in Table 1, except for the following:

- Operating temperatures: 1023 K for Case I, 1123 K for Case II, 1223 K for Case III, and 933 K for Case IV and V.
- Area-specific resistance (ASR): For Case I, ASR is 0.41 Ω•cm^2 in fuel cell mode and 0.55 Ω•cm^2 in electrolysis mode. For Case II, it is 0.16 in fuel cell mode and 0.26 Ω•cm^2 in electrolysis mode. For Case III, ASR is 0.35 Ω•cm^2 for electrolysis mode. For cases IV and V, ASR is 0.8 and 0.77 Ω•cm^2, respectively.
- Steam conversion ratio (SC) is 0.35 for electrolysis mode in cases I to III.
- Inlet fuel composition: 50 % H2 and 50 % H2O for Case I and Case II; 30 % H2 and 70 % H2O for Case III; 100 % methane for case IV; and 67 %H_2+33 % methane for case V.

The model incorporates constant losses attributed to activation, concentration, and ohmic effects, represented by the parameter ASR (area-specific resistance). The validation of the voltage-current density characteristic is illustrated in Fig. 2. The maximum error for cases 1 to 5 are 2.6 %, 3.1 %, 2.2 %, 1.42 %, and 1.16 % respectively. The average error of the modeling is 2.1 %.

5. Results and discussion

5.1. Fuel cell mode

5.1.1. Stack

The stack's operational current density (i_{op}) is a key factor in controlling its power output. With the stack running at a constant fuel utilization, i_{op} could be adjusted by modulating the feed flow rate. Fig. 3 illustrates the output power, operational voltage, stack efficiency, heat generation, and air ratio as functions of current. It is significant to mention that clear inverse relationship exists between the stack's operational voltage and the current density. According to Fig. 3-a, there is an inverse relationship between the operating voltage of the stack and

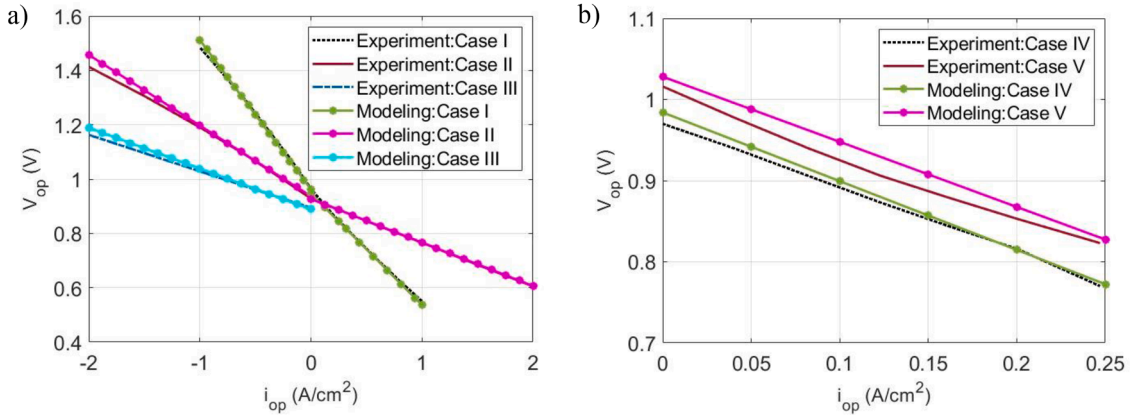

Fig. 2. Validation of RSOC model characteristics with experimental voltage-current density data, (a) with hydrogen fuel (Cases I to III), and (b) Fuel cell feed with methane and a combination of hydrogen and methane (Cases IV and V).

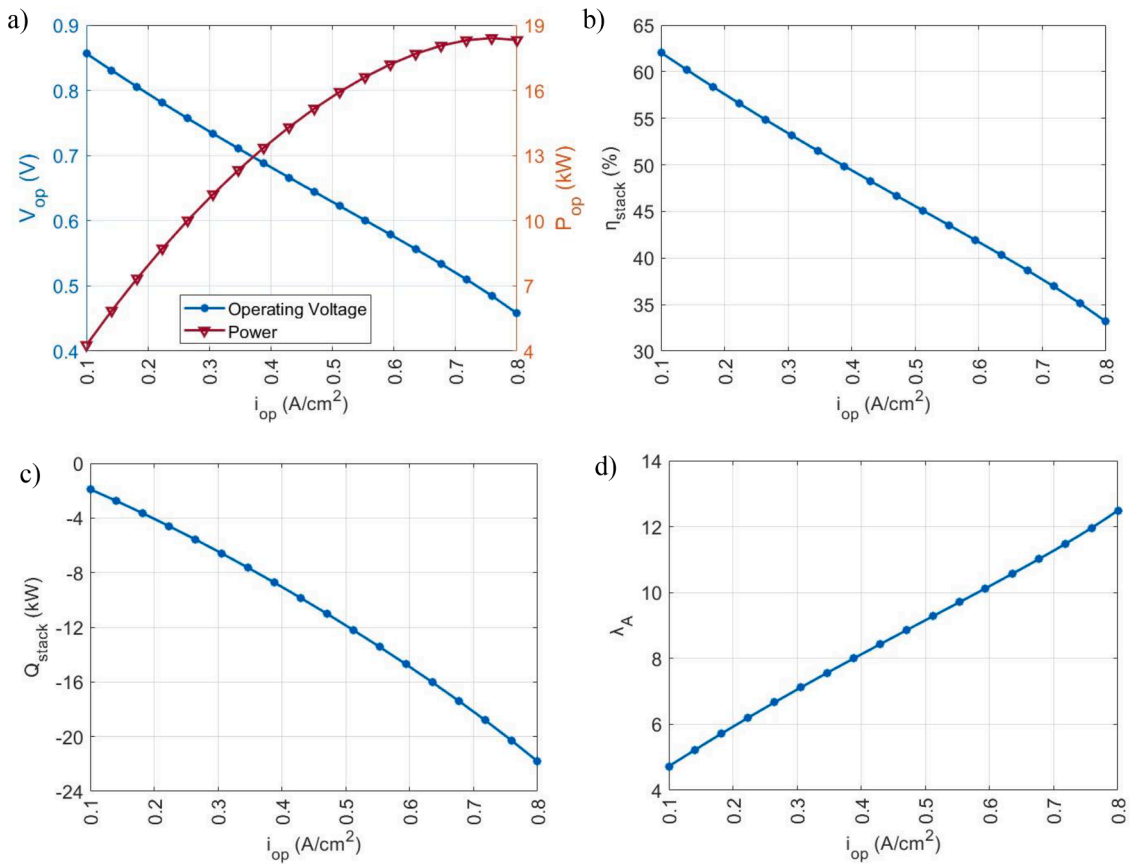

Fig. 3. Power and voltage (a), stack efficiency (b), generated heat (c), and air ratio (d) in fuel cell mode with methane as inlet fuel vs. current density.

the current density. The power density has a parabolic shape with respect to the current and it peaks at a power density of 18.4 kW at a current density of 0.76 A/cm2. Due to this inverse relationship, the operating currents of the RSOC should always be to the left of the peak power density. This analysis is essential for identifying the optimal operating point that balances power output and system durability. A comparison between the results of this study and those reported by Mojaver et al. [62] confirms that the trend of output power versus current density is consistent across both studies, reinforcing the reliability of the observed performance behavior. As depicted in Fig. 3-b, stack efficiency (η_{stack}) declines with increasing current density, ranging from 62.1 % to 33.2 %, amounting to 35.1 % at top power level. The study emphasizes that operational current densities should stay below the one corresponding to maximum power. Therefore, the current density range investigated in the present study spans from 0.1 to 0.8 A/cm^2, with no further exploration into higher current densities. Introducing an anode gas recycling stream improves stack efficiency, with a recirculation value of 0.6, allowing each H_2 molecule multiple opportunities for electricity conversion. Fig. 3-c shows that escalating the system's current corresponds to a rise in heat generation within the cell. The negative value of heat implies that it is being generated in the stack, not consumed. Maintaining a consistent average temperature (ΔT_{cell}) necessitates managing this increased heat generation by augmenting the volume of air passing inside the cathode. Heat generation by the stack (Q_{stack}) exhibits a nonlinear increase with current, ranging from 1.9 kW to 21.8 kW. Correspondingly, Fig. 3-d shows that the requisite air ratios (λ_A) escalate from 4.7 at 0.1 A/cm^2 to 12.5 at 0.8 A/cm^2.

5.1.2. Overall system

The performance of the system in fuel cell mode is significantly impacted by the ancillary power demand of the BoP elements, with

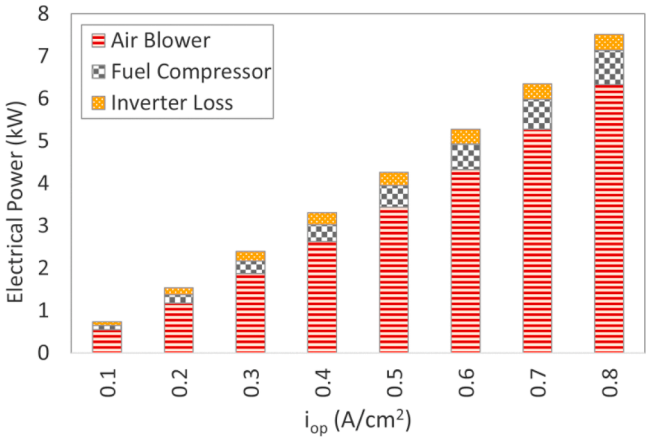

Fig. 4. Power of overall system's components in fuel cell mode.

parasitic losses reducing the net power production and overall system efficiency. The energy requirements of different components in fuel cell mode are delineated in Fig. 4. The primary parasitic losses come from the air blower, which circulates additional air to cool the stack, and its contribution to total losses increases from 75 % to 84 % as current density rises from 0.1 A/cm^2 to 0.8 A/cm. The fuel compressor accounts for the second-largest losses, with its share decreasing from 14 % to 11 % as current density increases from 0.1 A/cm^2 to 0.8 A/cm^2. Additionally, the inverter's share of losses is more significant at lower current densities, decreasing from 12 % to 5 %. This disparity arises because the inverter accounts for constant transformation inefficiencies. Consequently, with an increase in current density from 0.1 to 0.8 A/cm^2, the overall system efficiency in fuel cell mode declines from 59.4 % to 22.6

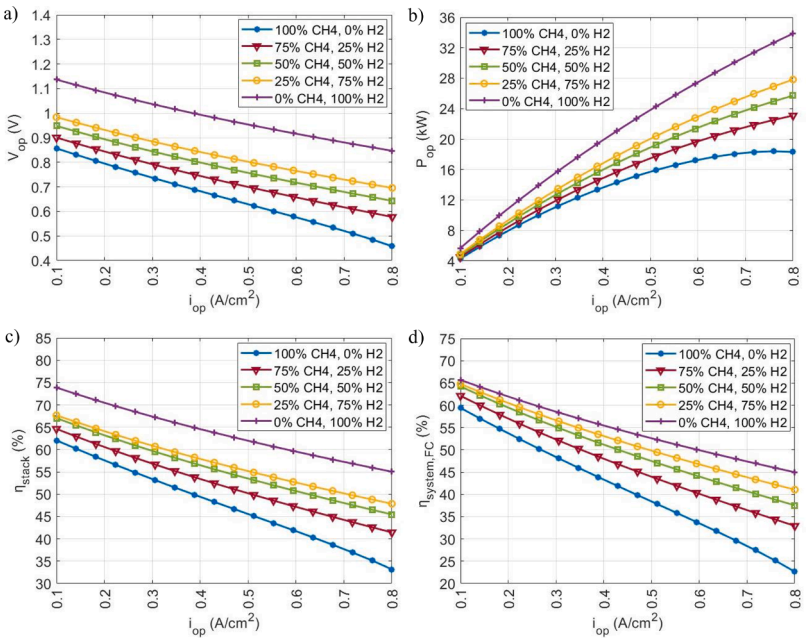

Fig. 5. Operating voltage (a), power (b), stack efficiency (c), and total system efficiency (d) vs. current density for different inlet fuels.

%.

5.1.3. Sensitivity to inlet fuel

To explore the impact of varying percentages of methane and hydrogen as inlet fuel on system operation, five gas compositions are analyzed. The compositions range from 100 % methane and 0 % hydrogen, gradually reducing the methane content by 25 % increments while correspondingly increasing the hydrogen content by the same percentage. All other inputs remain constant, as detailed in Table 1.

As depicted in Fig. 5-a, increasing the hydrogen content in the inlet fuel leads to a rise in generated voltage. This is primarily attributed to the faster kinetics of the hydrogen reaction, resulting in reduced activation losses and improved hydrogen diffusion into the porous electrode, consequently reducing concentration losses. Additionally, it is observed that the discrepancy between the curves intensifies with higher current densities, and the separation between the lines diminishes at lower current densities. The plot corresponding to the scenario where the input fuel comprises solely hydrogen exhibits a relatively greater distance from the other curves compared to scenarios with a carbon-containing input. This indicates that even a small percentage of carbon significantly reduces the generated voltage. Furthermore, the separation between the line corresponding to 100 % methane input fuel and those of hydrogen-methane mixtures is greater, suggesting that the initial increase of 25 % hydrogen in the input fuel has a more pronounced effect than subsequent increments. The maximum operating voltage in the case that inlet fuel is only hydrogen is 1.14 V while in the case of only methane as inlet fuel the value is 0.86 V.

Since the steam-to-carbon ratio parameter is considered constant, the value of recirculation rate is different in each case. It is equal to 0.6, 0.57, 0.5, 0.38, and 0 for the investigated compositions (from 100 % CH_4 to 100 % H_2), respectively. As the amount of inlet carbon decreases, the need for recirculation diminishes due to reduced risk of carbon deposition. Consequently, when the inlet fuel consists solely of hydrogen, recirculating a portion of the outlet stream becomes unnecessary.

According to Fig. 5-b, increasing the percentage of H_2 in the inlet fuel yields in a rise in generated power. In the examined range of current densities, the maximum power produced when the inlet fuel consists solely of hydrogen is 1.3–1.8 times higher compared to when the inlet fuel is solely methane. While increasing the current density beyond 0.76 A/cm² leads to a decrease in stack power output with methane input fuel, this trend no longer holds true with higher hydrogen content in the inlet fuel. Instead, the point at which power begins to decrease shifts, and increasing the current density actually boosts output power.

The efficiency of the stack when the input fuel is hydrogen surpasses that of the stack when the input fuel is solely methane by 11.8–21.8 % (Fig. 5-c). According to Eq. (16), two factors contribute to this increase. Firstly, the power output rises with the increase of hydrogen in the inlet fuel. Secondly, to maintain a specific current density, the molar flow rate of the initial inlet stream ($\dot{N}_{F1}$) increases with the hydrogen content in the fuel inlet. However, owing to the lower molar mass of hydrogen compared to methane, the mass flow rate of the inlet stream ($\dot{m}_{F1}$) diminishes. Moreover, the Lower Heating Value (LHV) of hydrogen exceeds that of methane. Consequently, these factors collectively enhance the energy of the inlet stream to the stack, leading to an efficiency boost.

The effectiveness of the entire system in fuel cell mode is contingent upon both stack performance and the power consumption of other components. With elevated hydrogen content in the inlet flow, the power associated with the compressor escalates, despite the decrease in the mass flow rate of the inlet fuel, owing to the higher density of methane relative to hydrogen. Conversely, the heat produced at the stack rises as the amount of hydrogen in the inlet fuel decreases. This can be attributed to three factors: firstly, the internal reformation process is endothermic. Secondly, in a certain current density, the molar flow rate of the inlet fuel increases with the rise in hydrogen content. Furthermore, hydrogen boasts a greater energy content than methane. Consequently, the demand for air for stack cooling amplifies along with the rise in hydrogen in the inlet fuel, causing a corresponding rise in the required power of the air blower. The increase in the required power of the blower ranges from 58 % to 72 % within the examined current density range. Given that the net output power is greater when the hydrogen content in the inlet fuel is enhanced, the power of the inverter also increases accordingly. As a result, the overall system efficiency sees an uptick as hydrogen levels rise in the inlet flow. Specifically, the efficiency of the overall system in the scenario that the input fuel is hydrogen exceeds that of the scenario where the input fuel is solely methane by 6.2–22.3 % (Fig. 5-d).

5.1.4. Sensitivity to fuel utilization factor (U_f)

Since fuel utilization is a key factor of the proposed system in fuel cell mode, it is essential to investigate its effect on both stack and overall

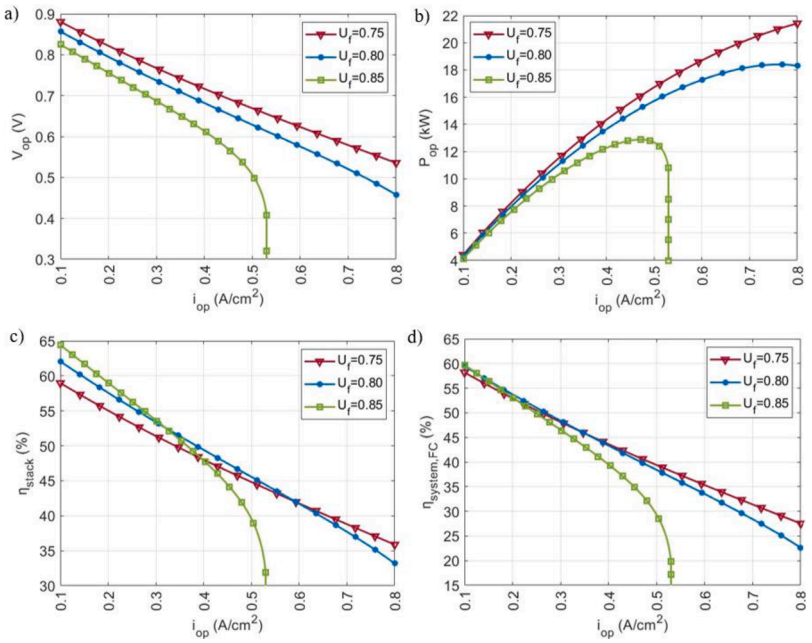

Fig. 6. Operating voltage (a), power (b), stack efficiency (c), and total system efficiency (d) vs. current density for different fuel utilization factor.

system performance. In this study, all base-case inputs remain constant. The only variable is the fuel utilization factor, which is adjusted from the base case value of 0.8 to 0.75 and 0.85. As seen in Fig. 6-a, operating SOFC with a higher fuel utilization factor leads to reduced operating voltages. As fuel utilization rises, the SOFC utilizes a larger portion of the produced H_2 from internal reforming, leading to a drop in operating voltage. The curve for $U_f = 0.85$ shows a sudden drop at current densities above 0.5 A/cm^2, reaching zero at 0.54 A/cm^2. This is due to the predominance of concentration losses at this current density. According to Fig. 6-b, reduced voltages lead to diminished power densities across all currents. Increasing the fuel utilization factor from 0.8 to 0.85 reduces the current density at which maximum power is produced from 0.76 A/cm^2 to 0.48 A/cm^2. The highest power produced under these conditions is 18.4 kW and 12.8 kW, respectively. At a fuel utilization factor of 0.75, the maximum power point occurs at current densities above 0.8 A/cm^2. Therefore, decreasing the fuel utilization factor allows for a broader range of current densities to be considered in the analyses. A comparison with the results of Mojaver et al. [63] shows a consistent trend in the influence of the fuel utilization factor on power output. In their study, increasing the utilization factor from 0.65 to 0.85 led to a decrease in the maximum output power from 480 kW to 270 kW. These results align with the findings of this study, where lower utilization factors not only extend the range of operable current densities but also lead to higher maximum power outputs.

In spite of these findings suggesting that working at reduced fuel utilizations may seem advantageous, it leads to lower stack efficiency (Fig. 6-c)., since a smaller portion of the ready fuel is transformed into electricity. This implies that if the system operates with low fuel utilization factor, higher methane level is needed to generate a specific quantity of power, which adversely affects the system's financial aspect. However, this pattern changes at higher current densities. Comparing the lines for U_f =0.85 and U_f =0.8, it is evident that stack efficiency is higher for the greater fuel utilization factor at current densities lower than 0.33 A/cm^2, but this changes beyond that point. The reason is that at current densities above 0.33 A/cm^2, the reduction in generated power surpasses the reduction in the input mass flow rate energy, results in a quicker decline in efficiency for U_f =0.85. Similarly, comparing U_f =0.8 and U_f =0.75, the current density at which stack efficiency exceeds that of the lower fuel utilization factor is 0.6 A/cm^2, due to the same aforementioned reasons.

The effect of the fuel utilization factor on whole system efficiency is illustrated in Fig. 6-d. It is evident that at lower current densities (below 0.23 A/cm^2), the fuel utilization factor has minimal impact on whole system efficiency. However, at current densities higher than this value, a rise in the fuel utilization factor leads to a drop in overall system efficiency. This phenomenon occurs because the reduced mass flow rate of the input stream lowers the power required by the compressor. However, rising the fuel utilization factor leads to higher heat production within the stack, necessitating excess airflow through the cathode channel. Consequently, the parasitic losses of the air blower increase, significantly impacting overall system efficiency.

5.1.5. *Sensitivity to steam-to-carbon ratio (μ)*

The steam-to-carbon ratio is a critical parameter influencing system performance. It serves to prevent carbon deposition, a key concern in system operation. The effect of the steam-to-carbon ratio on both stack and overall system performance is illustrated in Fig. 7. For consistency, all inputs remain constant according to the base case outlined in Table 1, with only the steam-to-carbon ratio adjusted, transitioning from the base value of 2.5 to alternate values of 2 and 3.

As depicted in Fig. 7-a, higher steam-to-carbon ratios adversely affect system performance. Lower values of this parameter result in reduced steam presence during the reforming reaction, potentially causing a greater concentration of hydrogen in the reformate gas. Consequently, there is an increase in reactants and, consequently, the produced voltage. This consequence is less significant at reduced current densities. but becomes increasingly significant as current density rises. When comparing stack voltages for the three investigated μ values, it is observed that at current densities below 0.76 A/cm^2, the change in produced voltage when transitioning from steam-to-carbon ratio 2 to 2.5 and from 2.5 to 3 is roughly similar, varying within the range of 0.01–0.03 V. However, for current densities exceeding 0.76 A/cm^2, the disparity between the lines for steam-to-carbon ratios 2.5 and 3 widens, reaching up to 0.07 V. Rising the steam-to-carbon ratio yields a comparable impact to that of the fuel utilization factor on the current density associated with the stack's maximum power output. In the scenario with $\mu = 3$, the current density at which the stack achieves highest power is 0.71 A/cm^2, a reduction in comparison with the base case (Fig. 7-b).

As it can be seen in Fig. 7-c and -d, increasing μ leads to a decrease in either stack efficiency and overall system efficiency. As μ increases, the

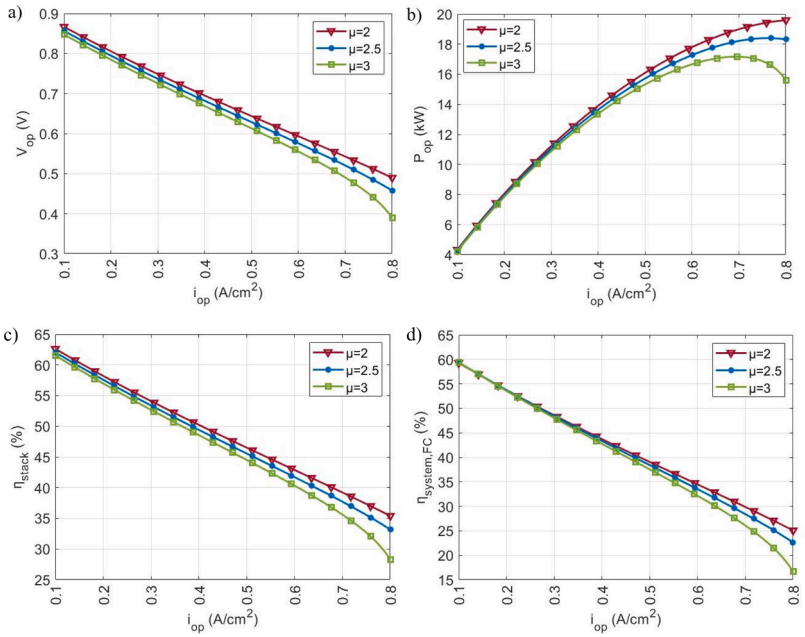

Fig. 7. Operating voltage (a), power (b), stack efficiency (c), and total system efficiency (d) vs. current density for different steam-to-carbon ratios.

mass flow rate of the input stream from the compressor decreases, leading to a reduction in the compressor's workload. However, the heat produced at the stack and the corresponding air needed for cooling increase, which in turn raises the workload of the air blower. Additionally, the power of the inverter is influenced by the generated power. The opposing effects of this factor on the compressor and air blower workload lead to a minimal overall impact on system efficiency. Consequently, changing μ from 2 to 3 results in an overall system efficiency variation of 0 to 8 % within the examined current density range.

5.1.6. *Sensitivity to operating temperature (T_{op})*

Operating temperature is another crucial parameter investigated in this study. All the inputs for the base-case, as presented in Table 1, remain constant, with only the operating temperature changing. In the base case, the operating temperature is adjusted to 1073 K, but it varies to 1023 K and 1123 K for further analysis. As depicted in Fig. 8-a, the operating voltage rises with a rise in operating temperature. This trend is attributed to lower activation and ohmic losses at higher temperatures. Consequently, Fig. 8-b shows that the power produced by the stack also rises with a rise in operating temperature. For example, at an operating temperature of 1023 K, the peak power reaches 13.9 kW, observed at a current density of 0.64 A/cm^2. Moreover, the power generated at 1123 K shows an overall increase across the entire range of investigated current densities.

Indeed, according to Fig. 8-c and -d, both stack and overall system efficiencies benefit from higher operating temperatures. However, the advantages of elevated temperatures are tempered by cost concerns and material thermal degradation. Increasing the operating temperature

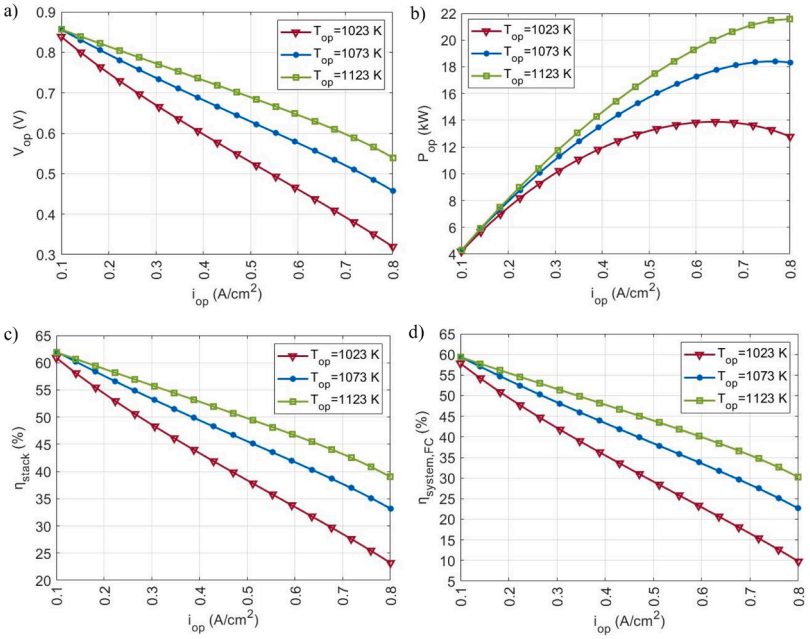

Fig. 8. Operating voltage (a), power (b), stack efficiency (c), and total system efficiency (d) vs. current density for different operating temperatures.

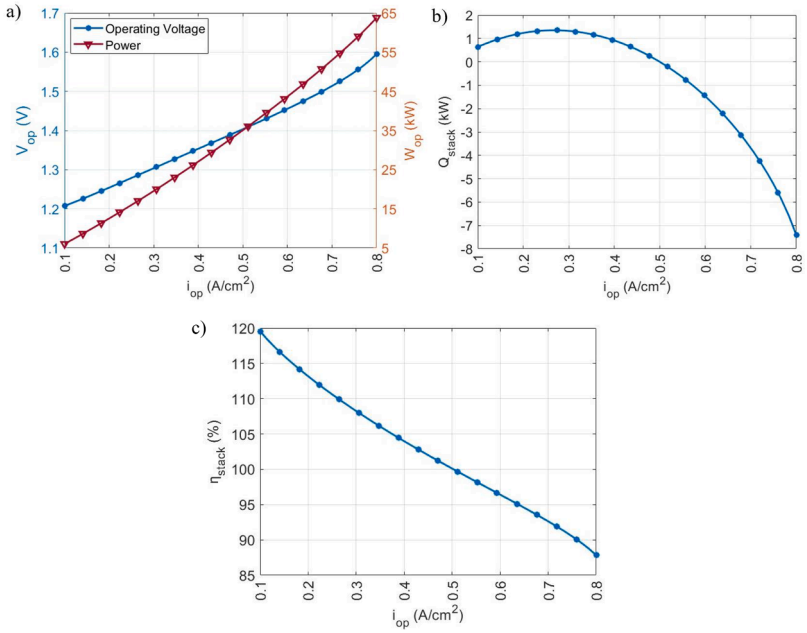

Fig. 9. Stack load and voltage (a), heat requirement (b) and stack efficiency (c) vs. current density in electrolysis mode.

from 1023 K to 1123 K results in a stack efficiency improvement ranging from 1 to 15.8 % across the examined current density range. While the compressor's power remains unaffected by changes in stack temperature, the increased heat generation by the stack necessitates greater cooling, thereby raising the workload of the air blower. Moreover, the power usage of the inverter also escalates. Nonetheless, the higher power output of the stack at elevated temperatures predominates these factors, resulting in an overall system efficiency increases with higher operating temperatures.

5.2. Electrolysis and methanation mode

5.2.1. Stack

In electrolysis mode, adjusting the system's output primarily relies on the operating current density as well. As illustrated in Fig. 9-a, the system's voltage spans from 1.2 to 1.6 V. With rising current density, both the stack's electricity consumption and operating voltage rise. Notably, in electrolysis mode, boosting the operating current invariably escalates power consumption. This arises because when the cell's polarity is reversed, its voltage consistently rises. Consequently, the stack's power demand surges alongside the voltage cell increment.

In Fig. 9-b the heat dynamics of the stack is depicted against the operating current density. Here, positive sign denotes heat usage by the stack (during endothermic mode), whereas negative sign indicates heat generation by the stack (during exothermic mode). The curve's nonlinear trajectory underscores the significance of energy equilibrium, as it directly influences the overall system efficiency. Fig. 9-c illustrates the efficiency of the stack relative to the operating current density. Certain operational currents display efficiencies exceeding 100 %. This peculiarity arises due to the possibility of operating below the thermoneutral point during electrolysis mode, resulting in an endothermic process. During such instances, efficiencies surpassing 100 % occur because the

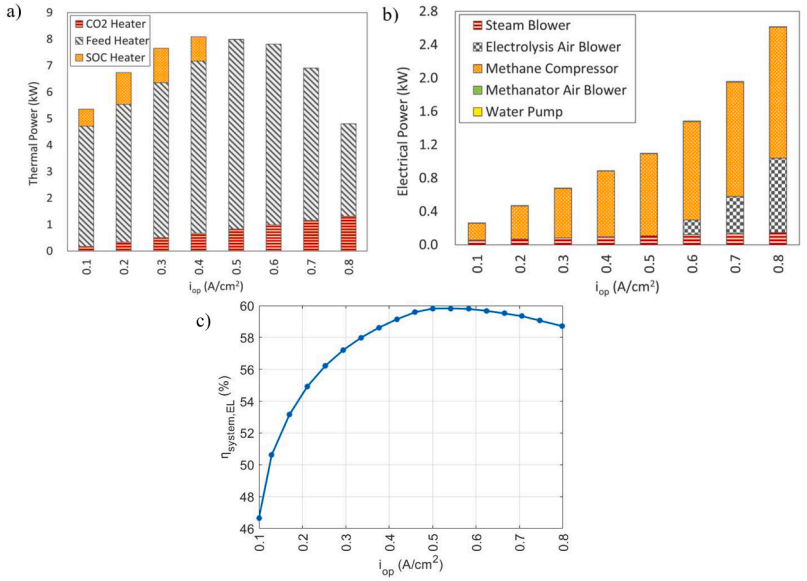

Fig. 10. External heating distribution (a), power distribution (b), and overall system efficiency vs. current density (c) in electrolysis mode.

traditional definition of stack efficiency neglects the heat needed to offset the decline in stack temperature caused by endothermic operations. If this heating load were accounted for, stack efficiencies would fall <100 % excluding the current corresponding to the thermoneutral voltage. At this point, exterior heating is not needed, resulting in an efficiency of 100 %.

5.2.2. Overall system

In the operational dynamics of electrolysis mode, the system undergoes a series of intricate processes. understanding the individual contributions of each element to the whole system efficiency is paramount. Fig. 10-a illustrates the required thermal power for different system components. The primary contributor to thermal power parasitic losses is the feed heater. As current rises and the process transitions from endothermic to exothermic, the thermal power of SOEC diminishes. Consequently, the total thermal power comprises the power needed to pre-heat CO_2 for the methanation reaction and the feed heating. In endothermic operation, the feed heating value rises with increasing current density, while in exothermic operation, it decreases. However, within the explored current density range, the heat produced at the stack in exothermic operation is insufficient to meet all the inlet stream heating requirements. In endothermic operation, the share of this parameter in the total thermal power parasitic losses increases from 85 % to 90 %, and then decreases from 90 % to 73 % as the operation mode changes to exothermic. Notably, the decreasing trend of feed heating suggests its eventual elimination at higher current densities. Additionally, the required thermal power for CO_2 heating increases with rising current, attributed to the heightened molar flow rate of inlet and outlet streams from the stack, leading to increased demand for CO_2 in the methanation reactor. The share of this parameter in the total thermal power parasitic losses changes between 3 % and 17 % as the current density increases from 0.1 to 0.8 A/cm^2.

The electrical power distribution of different components is depicted in Fig. 10-b. The required electrical powers for the water pump and air blower of the methanation unit are negligible. However, when the stack current rises and shifts the process from endothermic to exothermic, the electrical power associated with the electrolysis air blower emerges. With the stack becoming increasingly exothermic, the heat generated at the stack grows in a non-linear manner, necessitating greater quantities of air to pass from the oxygen electrode duct to maintain the stack temperature in acceptable limits. At a current density of 0.8 A/cm^2, 34 % of the total electrical power of the system is attributed to the electrolysis air blower. However, the methane compressor stands out as the major consumer of electrical power. As the amount of produced methane rises with rising current density, the power needed to achieve the network pressure also rises. Although the percentage of electrical power consumed by the methane compressor decreases from 78 % to 60 % within the examined current density range.

Changes in the overall system efficiency in electrolysis mode is illustrated in Fig. 10-c. As the current density escalates up to 0.5 A/cm^2, there is a corresponding uptick in the overall system efficiency. The pinnacle of overall system efficiency, reaching 59.8 %, is attained at the thermoneutral point. Nevertheless, as the current density surpasses 0.5 A/cm^2, the overall system efficiency commences a downturn, primarily attributable to the augmented electrical power of the air blower for stack cooling, despite the absence of thermal power required for SOC heating in this setup.

5.3. Roundtrip operation

The examination of roundtrip efficiency relies on the operational duration of RSOC in each mode. The roundtrip efficiencies of RSOC ($\eta_{RT,RSOC}$) and the overall system ($\eta_{RT,system}$) are illustrated in Fig. 11 assuming an equal duration for each operational mode. As depicted, $\eta_{RT,RSOC}$ experiences a declining trend as the current density rises, dropping from 70.9 % to 28.6 % across the examined range. For achieving higher $\eta_{RT,RSOC}$, it is advisable for the SOFC to operate at lower current densities while the SOEC at higher ones [59]. A comparison with the study by Santhanam et al. [10] further highlights the performance of the proposed system. At a current density of 0.25 A/cm^2, Santhanam et al. reported a roundtrip efficiency of 48 %, while at 0.15 A/cm^2 it reached 59 %. In contrast, the present study achieves significantly higher roundtrip efficiencies of 58 % and 68 % at the same current densities, respectively. This improvement is attributed to the larger temperature differential employed in the RSOC operation of this work. When compared to other energy storage technologies, RSOC's roundtrip efficiency typically ranges around 70 %, which is competitive with systems like Pumped Hydro Storage, which has an efficiency range of 70–85 %, and Flow Batteries with 84 %. However, RSOC stands out due to its scalability, fuel flexibility, and adaptability to renewable energy integration, making it a promising solution for long-duration energy storage applications.

Regarding roundtrip efficiencies of the overall system, it peaks at a current density of 0.14 A/cm^2. The low values are due to both SOFC and SOEC performances being evaluated at identical current densities. The implementation of the aforementioned changes in current density operations enhances this efficiency as well.

6. Conclusion

A novel energy system based on Reversible Solid Oxide Cell (RSOC) technology was proposed, capable of producing methane in electrolysis mode and low-carbon electricity in fuel cell mode. A zero-dimensional computational model was developed in MATLAB® to analyze both the stack and balance-of-plant (BoP) components in SOFC and SOEC modes.

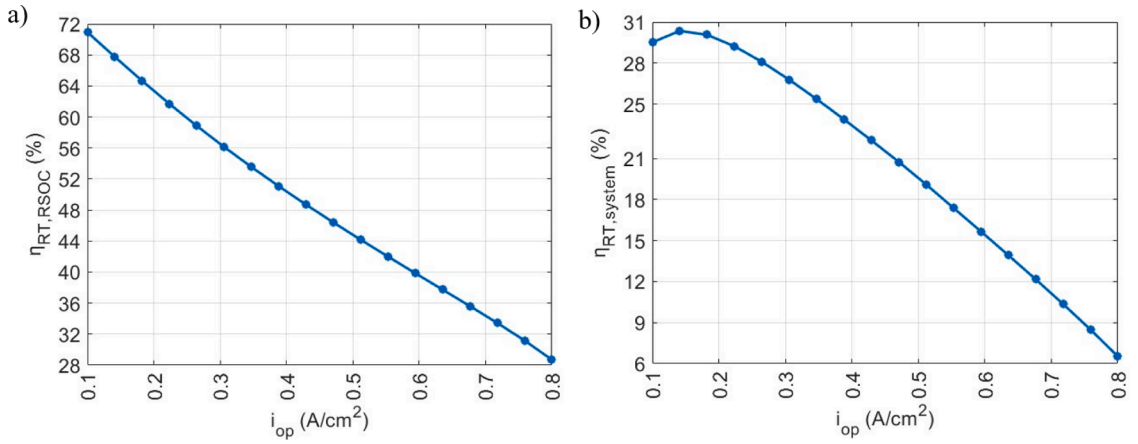

Fig. 11. Roundtrip efficiency of RSOC (a) and the overall system (b) vs. current density.

In SOFC mode:

- Stack efficiency varied from 33.2 % to 62.1 %, with 35.1 % observed at the point of maximum power.
- Overall system efficiency decreased from 59.4 % to 22.6 % as current density increased from 0.1 to 0.8 A/cm^2, primarily due to increased power consumption by auxiliary units, particularly the air blower.

Impact of fuel composition:

- Substituting methane with hydrogen as the inlet fuel resulted in a power output increase of 30 % to 80 %, depending on the operating current density.
- Stack efficiency was at least 11.8 % higher when using hydrogen.
- Overall system efficiency improved by 6.2 to 22.3 %, highlighting hydrogen's superior electrochemical performance compared to methane.

Fuel utilization, steam-to-carbon ratio, and operating temperature effects:

- Higher fuel utilization lowered cell voltage and power density; increasing utilization from 0.8 to 0.85 led to a 5.6 kW drop in maximum power.
- A higher steam-to-carbon ratio diluted the fuel mixture, reducing both cell voltage and system efficiency.
- Raising the operating temperature from 1023 K to 1123 K improved stack efficiency by up to 15.8 % due to reduced activation losses, although benefits were limited by cost and potential thermal degradation.

In SOEC mode:

- Higher current density increases power consumption, operating voltage, and heat generation.
- Below the thermoneutral point, the feed heater causes significant thermal power losses, while thermal energy is used to pre-heat CO2 and feed.
- As current density rises, electrical power demand increases for the air blower and methane compressor.
- Efficiency improves up to the thermoneutral point, after which it declines due to the need for additional cooling.

Roundtrip efficiency of RSOC:

- The roundtrip efficiency of RSOC decreases from 70.9 % to 28.6 % as current density increases.
- Overall system efficiency peaks at a current density of 0.14 A/cm^2.
- Efficiency improvement can be achieved by optimizing current density operations for both SOFC and SOEC.

The assumptions of steady-state, adiabatic, equilibrium, and uniform temperature conditions, which simplify the analysis in the current study, may not fully represent real system dynamics. These assumptions may overlook transient effects, heat losses, and non-equilibrium kinetics, particularly in methanation. Future work could incorporate these factors to improve the model's accuracy under varying operating conditions. Future research could also focus on integrating multi-fuel compositions, which may improve the model's adaptability to various fuel types and enhance its real-world applicability. Additionally, exploring cost-effectiveness and financial viability could offer valuable insights for policymakers and industry stakeholders.

CRediT authorship contribution statement

Zeinab Aghaziarati: Conceptualization, Methodology, Software, Validation, Formal analysis, Visualization, Writing – original draft. **Mohammad Ameri:** Conceptualization, Methodology, Writing – review & editing, Project administration, Resources, Supervision. **Mokhtar Bidi:** Conceptualization, Methodology, Investigation, Supervision. **Paolo Marocco:** Conceptualization, Writing – review & editing, Resources, Supervision. **Massimo Santarelli:** Writing – review & editing, Supervision. **Marta Gandiglio:** Conceptualization, Resources, Writing – review & editing, Funding acquisition, Supervision.

Declaration of competing interest

The authors declare that they have no known competing financial interests or personal relationships that could have appeared to influence the work reported in this paper.

Acknowledgements

This publication is partially funded by the NODES project, which has received funding from the MUR – M4C2 1.5 of PNRR, funded by the European Union – NextGenerationEU (Grant agreement no. ECS00000036).

Appendix A. mass flow rate modeling of RSOC

The molar flow rates of species j at both the inlet and outlet of the stack in fuel call mode are as follows [11]:

$$\dot{N}^{j}_{F4} = \dot{N}^{j}_{F2} + y^{j}_{P1}(r_{FC}\cdot\dot{N}_{P1}) \tag{A.1}$$

$$\dot{N}^{j}_{P1} = y^{j}_{P1}\cdot\dot{N}_{P1} \tag{A.2}$$

$$\dot{N}_{P2} = \dot{N}_{F4} - \dot{N}_{F2} \tag{A.3}$$

$$\dot{N}_{P3} = \dot{N}_{P1} - \dot{N}_{P2} \tag{A.4}$$

The recirculation rate is calculated using the following equation.

$$r_{FC} = \dot{N}_{P2} \Big/ \dot{N}_{P1} \tag{A.5}$$

Equations A.6 to A.10 outline the calculation process for determining the balanced gas mixture of the exit flow [11].

$$y_{P1}^{CH_4} = \frac{y_{F2}^{CH_4} \cdot \dot{N}_{F2} - \xi_{SMR}}{\dot{N}_{F2} + 2\xi_{SMR}} \tag{A.6}$$

$$y_{P1}^{H_2O} = \frac{y_{F2}^{H_2O} \cdot \dot{N}_{F2} - \xi_{SMR} - \xi_{WGS} + \xi_{redox}}{\dot{N}_{F2} + 2\xi_{SMR}} \tag{A.7}$$

$$y_{P1}^{H_2} = \frac{y_{F2}^{H_2} \cdot \dot{N}_{F2} + 3\xi_{SMR} + \xi_{WGS} - \xi_{redox}}{\dot{N}_{F2} + 2\xi_{SMR}} \tag{A.8}$$

$$y_{P1}^{CO_2} = \frac{y_{F2}^{CO_2} \cdot \dot{N}_{F2} + \xi_{WGS}}{\dot{N}_{F2} + 2\xi_{SMR}} \tag{A.9}$$

$$y_{P1}^{CO} = \frac{y_{F2}^{CO} \cdot \dot{N}_{F2} + \xi_{SMR} - \xi_{WGS}}{\dot{N}_{F2} + 2\xi_{SMR}} \tag{A.10}$$

In this context, ξ_{SMR}, ξ_{WGS}, and ξ_{redox} denote the molar extents of reactions corresponding to Eqs. (1) to 3, respectively. By expressing the molar flow rate of utilized H_2 (ξ_{redox}) in relation to the fuel utilization rate (U_f), it can be redefined using equation A.11. Fuel utilization rate is the ratio of the amount of fuel used in the fuel cell to the total amount of fuel supplied. Following some algebraic transformation, ξ_{redox} is expressed concerning the molar flow rate of the inlet flow ($\dot{N}_{F2}$) as described in equation A.12 [11].

$$\xi_{redox} = \left(\dot{N}_{F4}^{H_2} + 3\xi_{SMR} + \xi_{WGS}\right).U_f \tag{A.11}$$

$$\xi_{redox} = \frac{y_{F1}^{H_2} \cdot \dot{N}_{F1} + 3\xi_{SMR} + \xi_{WGS}}{1 - r_{FC} + r_{FC}.U_f} \tag{A.12}$$

Upon substituting equation A.12 into equations A.6 -A.10 and performing simplification, the equilibrium mole fraction of species can be expressed in terms of four unknowns: ξ_{SMR},ξ_{WGS},$r_{FC}$and $\dot{N}_{F2}$ [11]:

$$y_{P1}^{CH_4} = \frac{y_{F2}^{CH_4} \cdot \dot{N}_{F2} - \xi_{SMR}}{\dot{N}_{F2} + 2\xi_{SMR}} \tag{A.13}$$

$$y_{P1}^{H_2O} = y_{F2}^{H_2O} \cdot \frac{\dot{N}_{F2} - \xi_{SMR} - \xi_{WGS} + \frac{y_{F2}^{H_2} \cdot \dot{N}_{F2} + 3\xi_{SMR} + \xi_{WGS}}{1 - r_{FC} + r_{FC} \cdot U_f}}{\dot{N}_{F2} + 2\xi_{SMR}} \tag{A.14}$$

$$y_{P1}^{H_2} = \frac{y_{F2}^{H_2} \cdot \dot{N}_{F2} + 3\xi_{SMR} + \xi_{WGS}}{\dot{N}_{F2} + 2\xi_{SMR}} \cdot \left[\frac{(1 - r_{FC}) \cdot (1 - U_f)}{1 - r_{FC} + r_{FC} \cdot U_f}\right] \tag{A.15}$$

$$y_{P1}^{CO_2} = \frac{y_{F2}^{CO_2} \cdot \dot{N}_{F2} + \xi_{WGS}}{\dot{N}_{F2} + 2\xi_{SMR}} \tag{A.16}$$

$$y_{P1}^{CO} = \frac{y_{F2}^{CO} \cdot \dot{N}_{F2} + \xi_{SMR} - \xi_{WGS}}{\dot{N}_{F2} + 2\xi_{SMR}} \tag{A.17}$$

The combination of chemical equilibrium equations for steam reforming and water-gas shift, along with Faraday's law, yields a group of four separate equations utilized to figure out for ξ_{SMR},ξ_{WGS},$r_{FC}$and $\dot{N}_{F2}$ [11].

$$K_{SMR}(T) = \frac{y_{P1}^{CO} \cdot \left(y_{P1}^{H_2}\right)^3}{y_{P1}^{H_2O} \cdot y_{P1}^{CH_4}} \tag{A.18}$$

$$K_{WGS}(T) = \frac{y_{P1}^{H_2} \cdot y_{P1}^{CO_2}}{y_{P1}^{H_2O} \cdot y_{P1}^{CO}} \tag{A.19}$$

$$I_{cell} = 2F.\frac{y_{F2}^{H_2} \cdot \dot{N}_{F2} + 3\xi_{SMR} + \xi_{WGS}}{1 - r_{FC} + r_{FC}.U_f} \tag{A.20}$$

$$y_{F2}^{H_2O} \cdot \dot{N}_{F2} + \frac{2.y_{P1}^{H_2O}.\xi_{SMR} + r_{FC}.\dot{N}_{F2}}{1 - r_{FC}} = \mu.\left(y_{F2}^{CH_4} \cdot \dot{N}_{F2} + \frac{2.y_{P1}^{CH4}.\xi_{SMR} + r_{FC}.\dot{N}_{F2}}{1 - r_{FC}}\right) \tag{A.21}$$

The equilibrium coefficients for reactions 1 and 2, denoted as K_{SMR} and K_{WGS} respectively, are dependent on the operating temperature. They are computed utilizing the equation A.22 [56] where the coefficients C1-C5 are tabulated in Table A.1.

$$logK_P = C_1 T_{op}^{\ 4} + C_2 T_{op}^{\ 3} + C_3 T_{op}^{\ 2} + C_4 T_{op} + C_5 \tag{A.22}$$

Table A.1
Equilibrium constant coefficient [56].

	Reforming (SMR)	Shift (WGS)
C_1	$-2.63121 \cdot 10^{-11}$	$5.47301 \cdot 10^{-12}$
C_2	$1.24065 \cdot 10^{-7}$	$-2.57479 \cdot 10^{-8}$
C_3	$-2.25232 \cdot 10^{-4}$	$4.63742 \cdot 10^{-5}$
C_4	$1.95028 \cdot 10^{-1}$	$-3.91500 \cdot 10^{-2}$
C_5	$-6.61395 \cdot 10^{1}$	$1.32097 \cdot 10^{1}$

Equations A.23 to A.33 provide the basis for calculating the molar flow rate and the molar fractions of components across different streams in electrolysis mode [57].

$$\dot{N}_{F6} = \left[\frac{(1-r_{EL})\cdot\xi_{EL}}{SC} + SC\cdot r_{EL}\right]\cdot\left(\frac{1}{y_{F6}^{H_2O}}\right) \tag{A.23}$$

$$\dot{N}_{F8} = \frac{\dot{N}_{F6}}{1-r_{EL}} \tag{A.24}$$

$$y_{F8}^{H_2O} = \frac{y_{F6}^{H_2O}\cdot\dot{N}_{F6} - r_{EL}\cdot\xi_{EL}}{\dot{N}_{F6}} \tag{A.25}$$

$$y_{F8}^{H_2} = \frac{y_{F6}^{H_2}\cdot\dot{N}_{F6} - r_{EL}\cdot\xi_{EL}}{\dot{N}_{F6}} \tag{A.26}$$

$$\dot{N}_{P1} = \frac{\dot{N}_{F6}}{1-r_{EL}} \tag{A.27}$$

$$y_{P1}^{H_2O} = \frac{y_{F6}^{H_2O}\cdot\dot{N}_{F6} - r_{EL}\cdot\xi_{EL}}{\dot{N}_{F6}} \tag{A.28}$$

$$y_{P1}^{H_2} = \frac{y_{F6}^{H_2}\cdot\dot{N}_{F6} - r_{EL}\cdot\xi_{EL}}{\dot{N}_{F6}} \tag{A.29}$$

$$\dot{N}_{P2} = \frac{\dot{N}_{F6}\cdot r_{EL}}{1-r_{EL}} \tag{A.30}$$

$$y_{P2}^{j} = y_{P1}^{j} \tag{A.31}$$

$$\dot{N}_{P3} = \dot{N}_{P1} - \dot{N}_{P2} \tag{A.32}$$

$$y_{P3}^{j} = y_{P1}^{j} \tag{A.33}$$

Appendix B. overpotentials calculation

Ohmic losses (V_{ohmic}) are associated with the migration of ions and electrons within the cell. The overpotential resulting from ohmic loss is established by the current density, conductivity of the materials, and the length of the path that ions must travel. The terms δ and σ correspond to the thickness and conductivity of the operational layers. Equation B.2 provides the relationship for the conductivity of the operational layers [55].

$$V_{ohmic} = \left(\frac{\delta_{fuel\ electrode}}{\sigma_{fuel\ electrode}} + \frac{\delta_{air\ electrode}}{\sigma_{air\ electrode}} + \frac{\delta_{electrolyte}}{\sigma_{electrolyte}}\right) * i_{op} \tag{B.1}$$

$$\sigma_j = \sigma_{0,j}.\exp\left(\frac{-E_{activation}}{T_{op}}\right) \tag{B.2}$$

σ_0 is the specific conductivity at reference condition and $E_{activation}$ denotes the activation energy for oxidation or reduction reactions. Activation losses ($V_{activation}$) arise from the charge transfer that occurs at the onset of the system's operation at low currents. Typically, it is assessed using the Butler-Volmer equation. The simplified configuration of the equation utilized in this study is presented in equations B.4 and B.5 for fuel and air electrodes, respectively [55].

$$V_{activation} = V_{activation,\ fuel\ electrode} + V_{activation,\ air\ electrode} \tag{B.3}$$

$$V_{activation,\ fuel\ electrode} = \frac{R.T_{op}}{F}.\left(\sinh^{-1}\left(i_{op} \,/\, 2.i_{0,fuel\ electrode}\right)\right) \tag{B.4}$$

$$V_{activation,\ air\ electrode} = \frac{R.T_{op}}{F}.\left(\sinh^{-1}\left(i_{op} \,/\, 2.i_{0,air\ electrode}\right)\right) \tag{B.5}$$

i_0 represents exchange current density for fuel and air electrodes, calculated using equations B.6 and B.7. ϕ denotes frequency factor of the electrode reactions, while y^{j}_{ave} signifies the average molar fraction of species j of the inlet and outlet flows.

$$i_{0,fuel\ electrode} = \phi_{fuel\ electrode}.y^{H2}_{ave}.y^{H2O}_{ave}.\exp\left(\frac{-E_{activation,fuel\ electrode}}{R.T_{op}}\right) \tag{B.6}$$

$$i_{0,air\ electrode} = \phi_{air\ electrode}.{y^{O2}_{ave}}^{0.25}.\exp\left(\frac{-E_{activation,air\ electrode}}{R.T_{op}}\right) \tag{B.7}$$

Concentration losses ($V_{concentration}$) encompass losses stemming from resistance to mass movement from flow passages to the active locations. The electrochemical reactions occur at the junctions between the electrolyte and electrodes, requiring the diffusion of substances to the active locations through the permeable electrodes. The electrochemical reactions at these locations induce intensity gradients over the electrodes, driving the diffusion movement process [55].

$$V_{concentration} = V_{concentration,\ fuel\ electrode} + V_{concentration,\ air\ electrode} \tag{B.8}$$

$$V_{concentration,\ fuel\ electrode} = \frac{R.T_{op}}{2F}.\ln\left(\frac{y^{H2O}_{TPB}.y^{H2}_{bulk}}{y^{H2O}_{bulk}.y^{H2}_{TPB}}\right) \tag{B.9}$$

$$V_{concentration,\ air\ electrode} = \frac{R.T_{op}}{4F}.\ln\left(\frac{y^{O2}_{bulk}}{y^{O2}_{TPB}}\right) \tag{B.10}$$

y^{j}_{bulk} and y^{j}_{TPB} are mole fraction of species j at bulk and three phase boundary (TPB) points, respectively. They can be calculated as follows [64]:

$$y^{H2O}_{TPB} = y^{H2O}_{s} + \frac{R.T_{op}.i_{op}.\delta_{fuel\ electrode}}{2F.P_{cell}.D_{eff,\ H2O}} \tag{B.11}$$

$$y^{H2}_{TPB} = y^{H2}_{s} - \frac{R.T_{op}.i_{op}.\delta_{fuel\ electrode}}{2F.P_{cell}.D_{eff,\ H2}} \tag{B.12}$$

$$y^{O2}_{TPB} = 1 + \left(y^{O2}_{s} - 1\right).\exp\left(\frac{R.T_{op}.i_{op}.\delta_{air\ electrode}}{4F.P_{cell}.D_{eff,O2}}\right) \tag{B.13}$$

y^{j}_{s} represents the molar fraction of species j on the exterior area of the electrode and is calculated as follow [64]:

$$y^{H2O}_{s} = y^{H2O}_{bulk} + \frac{R.T_{op}.i_{op}.\left(\frac{\delta_{fuel\ electrode}}{2}\right)}{2F.P_{cell}.D_{H2,H2O}} \tag{B.14}$$

$$y^{H2}_{s} = y^{H2}_{bulk} + \frac{R.T_{op}.i_{op}.\left(\frac{\delta_{fuel\ electrode}}{2}\right)}{2F.P_{cell}.D_{H2,H2O}} \tag{B.15}$$

$$y^{O2}_{s} = 1 + \left(y^{O2}_{bulk} - 1\right).\exp\left(\frac{R.T_{op}.i_{op}.(\delta_{air\ electrode}/2)}{4F.P_{cell}.D_{O2,N2}}\right) \tag{B.16}$$

Equations B.17-B.19 provide the effective diffusion coefficient for different species [52].

$$D_{eff,\ H2O} = \frac{\xi}{\theta}.\left(\frac{1}{D_{H2,H2O}} + \frac{1}{D_{H2O,K}}\right) \tag{B.17}$$

$$D_{eff,\ H2} = \frac{\xi}{\theta}.\left(\frac{1}{D_{H2,H2O}} + \frac{1}{D_{H2,K}}\right) \tag{B.18}$$

$$D_{eff,\ O2} = \frac{\xi}{\theta}.\left(\frac{1}{D_{O2,N2}} + \frac{1}{D_{O2,K}}\right) \tag{B.19}$$

ξ and θ are the tortuosity and porosity, respectively. $D_{i,j}$ which denotes the molecular migration of species i in the species j is stated in equations B.20 -B.25. $D_{j,K}$ stands for the Knudsen diffusion coefficient for species j which can be determined using equation B.26 [52].

$$D_{i,j} = \frac{0.0000266{T_{op}}^{1.5}}{P_{cell}.{M_{i,j}}^{0.5}.{\sigma_{i,j}}^{2}.\Omega_{D}} \tag{B.20}$$

$$M_{i,j} = 2.\left(\frac{1}{M_i} + \frac{1}{M_j}\right)^{-} \tag{B.21}$$

$$\sigma_{i,j} = \frac{\sigma_i + \sigma_j}{2} \tag{B.22}$$

$$\Omega_D = \frac{1.06036}{\Gamma^{0.15610}} + \frac{0.19300}{\exp(0.47635\Gamma)} + \frac{1.03587}{\exp(1.52996\Gamma)} + \frac{1.76474}{\exp(3.89411\Gamma)} \tag{B.23}$$

$$\Gamma = \frac{T_{cell}}{\epsilon_{i,j}} \tag{B.24}$$

$$\epsilon_{i,j} = \sqrt{\frac{\epsilon_i}{k_B}\frac{\epsilon_j}{k_B}} \tag{B.25}$$

$$D_{j,K} = \frac{d_p}{3}\sqrt{\frac{8000.R.T_{op}}{\Pi M_j}} \tag{B.26}$$

M, $\sigma_{i,j}$, Ω_D, Γ, $\varepsilon_{i,j}$, k_B, and d_p are molecular weight, mean characteristic length of species i and j, diffusion collision integral, dimensionless temperature coefficient, Lennard-Jones energy, Boltzmann's constant, and mean pore size, respectively. Table B.1 represents the primary parameters for effective diffusion coefficient calculations [55].

Table B.1
Parameters for diffusion calculation [55].

	H_2O	H_2	O_2	N_2
σ_i	2.641	2.827	3.467	3.798
$\frac{\epsilon_i}{k_B}$	809.1	59.7	106.7	71.4

Appendix C. modeling of BoP

Pumps and blowers

Pumps and blowers play a crucial role in circulating liquid water or air throughout the system in fuel cell as well as electrolysis modes. They are modeled as processes with constant isentropic efficiency. The power needed for the pumps and blowers can be calculated using equation C.1, where v represents the volumetric flow rate of the liquid or air, and $\Delta P_{pump/blower}$ denotes the required pressure rise [65]. This elevation can be estimated by considering unique pressure reductions across different system elements.

$$W_{\text{pump/blower}} = \frac{v \cdot \Delta P_{pump/blower}}{\eta_{is,pump/blower}} \tag{C.1}$$

Compressor

A compressor is employed in fuel cell mode to elevate the pressure of the feed, facilitating its ability to counteract pressure decreases throughout the system. Additionally, a compressor is utilized in electrolysis mode to compress the produced CH_4 to meet the necessary temperature and pressure for introduction to the gas distribution network.

Equations C.2 and C.3 are employed to calculate the power for the compressor and the final discharge temperature of the compressor ($T_{out,comp}$). Here, γ denotes the molar heat capacity ratio of the fluid (c_p/c_v) and M_{fluid} represents the molar weight of the fluid. T_{comp} indicates the temperature at which the compressor operates, while $P_{out,comp}$ and $P_{in,comp}$ indicate the outlet and inlet pressures of the compressor, respectively. η_{mech} and $\eta_{is,\text{comp}}$ signify the mechanical and isentropic efficiencies of the compressor [66].

$$W_{compressor} = \frac{\gamma}{\gamma - 1}\left(\frac{RT_{comp}}{M_{fluid}\eta_{mech,comp}}\right)\left(\frac{P_{out,comp}}{P_{in,comp}}\right)^{\frac{\gamma}{\gamma-1}} \tag{C.2}$$

$$T_{out,comp} = T_{in,comp}\left[1 + \frac{\left(\frac{P_{out,comp}}{P_{in,comp}}\right)^{\frac{\gamma}{\gamma-1}} - 1}{\eta_{is,\text{comp}}}\right] \tag{C.3}$$

Pre-heaters

Pre-heaters are presumed to operate as planar counterflow heat exchangers. During the modeling process, the cold streams temperatures at inlet and outlet of the heat exchanger ($T_{c,in}$ and $T_{c,out}$), along with the initial temperature of the hot flow ($T_{h,in}$), are already identified based on the modeling of other components. Hence, the exit temperature of the hot flow ($T_{h,out}$) could be derived by equation C.5, obtained from an energy balance around the pre-heater. Here, $\dot{m}_c$ and $\dot{m}_h$ denote mass flow rates of cold and hot streams, respectively, while $h_{c,in}$ and $h_{c,out}$ represent the specific enthalpies of the

cold stream at entrance and exit. Additionally, c_p indicates the specific heat capacity of the hot stream.

$$Q_{pre\_heater} = \dot{m}_c \cdot (h_{c,\ out} - h_{c,\ in}) \tag{C.4}$$

$$T_{h,\ out} = T_{h,\ in} - \frac{Q_{pre\_heater}}{\dot{m}_h \cdot c_p} \tag{C.5}$$

Catalytic combustor

The combustion reactions are as follow:

$$CH_4 + 2O_2 \rightarrow CO_2 + 2H_2O \tag{C.6}$$

$$CO + \frac{1}{2}O_2 \rightarrow CO_2 \tag{C.7}$$

$$H_2 + \frac{1}{2}O_2 \rightarrow H_2O \tag{C.8}$$

According to [67], near 1073 K, a complete conversion of the unconsumed anode gases is observed. The paper notes the highest operating temperature of 850 °C, beyond which the catalyst's performance decreases, leading to permanent harm. Hence, the combustor adopts a maximum temperature (T_{comb}) of 1123 K for the flue gas exiting the combustor. Oxygen needed for combustion is sourced by blending the exit flow of the oxygen channel, which includes additional air utilized to regulate the temperature difference inside the cell. Given that all combustion mechanisms proceed to completion, The thermal energy liberated during combustion ($Q_{combustio}$) is determined using equation C.9. The terms ΔH_{rxn_m}, ΔH_{rxn_c} and ΔH_{rxn_h} denote the heats of reactions for reactions C.6, C.7, and C.8, respectively. To maintain isothermal operation, the quantity of cold bypassed air ($\dot{m}_{A4}$) can be calculated using equation C.10.

$$Q_{combustion} = \dot{m}_{P3}^{CH4} \cdot \Delta H_{rxn\_m} + \dot{m}_{P3}^{CO} \cdot \Delta h_{rxn\_c} + \dot{m}_{P3}^{H2} \cdot \Delta h_{rxn\_h} \tag{C.9}$$

$$\dot{m}_{A4} = \frac{-Q_{combustion}}{h_{A,c} - h_{A,o}} \tag{C.10}$$

$h_{A,c}$ and $h_{A,o}$ denote the specific enthalpy of air at the combustor temperature and at the ambient temperature, respectively. The gas outlet composition is determined using the following equations:

$$\dot{n}_{P4}^{CH4} = 0 \tag{C.11}$$

$$\dot{n}_{P4}^{H2} = 0 \tag{C.12}$$

$$\dot{n}_{P4}^{CO} = 0 \tag{C.13}$$

$$\dot{n}_{P4}^{CO2} = \dot{n}_{P3}^{CO2} + \dot{n}_{P3}^{CH4} + \dot{n}_{P3}^{CO} \tag{C.14}$$

$$\dot{n}_{P4}^{H2O} = \dot{n}_{P3}^{H2O} + 2\,\dot{n}_{P3}^{CH4} + \dot{n}_{P3}^{H2} \tag{C.15}$$

$$\dot{n}_{P4}^{O2} = \dot{n}_{A6}^{O2} + 0.21\,\dot{n}_{A4} - 2\dot{n}_{P3}^{CH4} - 0.5\,\dot{n}_{P3}^{CO} - 0.5\dot{n}_{P3}^{H2} \tag{C.16}$$

$$\dot{n}_{P4}^{N2} = \dot{n}_{A6}^{N2} + 0.79\dot{n}_{A4} \tag{C.17}$$

Evaporator

It is assumed that water is supplied in its liquid phase at 373 K, and saturated vapor is discharged at the same temperature. Therefore, the energy needed for steam creation can be determined using equation C.18, Where Δh_{evap} represents the heat required for water to vaporize. In cases where the total available waste heat from methanation and the air electrode side of the stack are insufficient to meet the required energy for steam formation, a feed electrical heater is employed to supply the remaining amount of required energy. The feed electrical heater is modeled similarly to other electrical heaters within the overall system.

$$Q_{evaporator} = \dot{m}_{F3} \cdot \Delta h_{evap} \tag{C.18}$$

Electrical heater/ cooler

During electrolysis mode, electric heaters are utilized to provide heating or cooling to specific processes or units where waste heat is unavailable or insufficient. The energy required by the electric heater ($W_{el,heater}$) can be calculated from equation C.19. Here, $Q_{required}$ represents the heating or cooling demand that the electrical device must fulfill, and η_{el} denotes the efficiency of the electric heater.

$$W_{el,heater} = \frac{Q_{required}}{\eta_{el}} \tag{C.19}$$

Methanation reactor

In the methanation reactor, the reaction described by equation C.20 occurs:

$$CO_2 + 4H_2 \rightarrow CH_4 + 2H_2O \tag{C.20}$$

For effective CO_2 hydrogenation, a significant surplus of hydrogen compared to carbon is essential, typically at a ratio of at least 4:1 [46]. This process is characterized by its notable heat release, which should be managed by transferring the reaction heat to an air stream. In the modeling, it is supposed that a constant temperature rise exists between the entrance and exit of the methanation unit flows. The reaction takes place at a temperature, which equals the average of the entrance and exit flows temperatures.

The heat generated during methanation can be computed using equation C.21, where $\dot{m}^j_{P7}$ and $\dot{m}^j_{P6}$ represent the flow rate of species j at the entrance and exit of the methanation reactor, and h^j_{P7} and h^j_{P6} denote the specific enthalpies of species j at the exit and entrance of the reactor. ξ_{meth} is the molar extent of the methanation reaction, that can be calculated from equation C.22. ΔH_{rxn_meth} represents the standard enthalpy change for the methanation reaction.

The required airflow for methanation ($\dot{m}_{A7}$) is determined by equation C.23, where $c_{p,A}$ is the heat capacity of air at the reaction temperature, and $\Delta T_A$is the temperature difference between the entrance and exit air flows.

$$Q_{methanation} = \sum \dot{m}^j_{P6} h^j_{P6} - \dot{m}^j_{P5} h^j_{P5} + \xi_{meth} \cdot \Delta H_{rxn\_meth} \tag{C.21}$$

$$\xi_{meth} = \dot{n}^{CH4}_{P6} - \dot{n}^{CH4}_{P5} \tag{C.22}$$

$$\dot{m}_{A7} = \frac{Q_{methanation}}{c_{p,A} \cdot \Delta T_A} \tag{C.23}$$

Methanation reactions are kinetically limited at low temperatures and require metal-based catalysts [68]. Ni is most commonly used, though Ru and other metals are also employed due to their high activity, especially at lower temperatures [69]. Catalyst performance is influenced by factors like metal loading and support material, with Al_2O_3 being a typical choice. However, high temperatures and CO-rich feeds can lead to deactivation [68]. In this study, we assume ideal catalytic behavior and sufficiently fast kinetics to justify a thermodynamic approach, with the reaction taking place isothermally at the average temperature of the inlet and outlet flows. This simplification is consistent with recent designs like heat-exchanger-assisted reactors, which manage heat efficiently and are suitable for small-scale applications [70].

Water separator

In electrolysis mode, before compressing methane for grid introduction, the steam and water produced in the methanation unit must be divided. Water is extracted from the outlet flow via condensation in a flash tank. At temperatures below 323 K, the vapor phase contains <5 % H_2O [47]. Thus, the flash tank is considered to operate at a steady temperature. Energy balance is then applied using equation C.24, Where $h^j_{T_{flash}}$ and $h^j_{T_{P6}}$ are the specific enthalpy of species j at the operating temperature of flash and at the inlet temperature, respectively. Δh_{cond} is the enthalpy of condensation.

$$Q_{flash} = \sum \dot{m}^j_{P6} \cdot \left(h^j_{T_{flash}} - h^j_{T_{P6}} \right) - \dot{m}_{H2O} \cdot \Delta h_{cond} \tag{C.24}$$

Inverter

When operating in fuel cell mode, the RSOC produces DC power, whereas in electrolysis mode, it consumes AC power. As the system interfaces with an external grid, any generated or consumed power needs rectification. To achieve this, an inverter is utilized for DC-to-AC conversion, accounting for fixed conversion losses.

Data availability

The data that has been used is confidential.

References

[1] M. Soltani, A. Hajizadeh Aghdam, Z. Aghaziarati, Design, fabrication and performance assessment of a novel portable solar-based poly-generation system, Renew. Energy 202 (2023) 699–712.

[2] S. Srikanth, M.P. Heddrich, S. Gupta, K.A. Friedrich, Transient reversible solid oxide cell reactor operation – experimentally validated modeling and analysis, Appl. Energy 232 (2018) 473–488.

[3] A. Buttler, H. Spliethoff, Current status of water electrolysis for energy storage, grid balancing and sector coupling via power-to-gas and power-to-liquids: a review, Renew. Sustain. Energy Rev. 82 (2018) 2440–2454.

[4] P. Kazempoor, R.J. Braun, Model validation and performance analysis of regenerative solid oxide cells for energy storage applications: reversible operation, Int. J. Hydrog. Energy 39 (11) (2014) 5955–5971.

[5] P. Mottaghizadeh, S. Santhanam, M.P. Heddrich, K.A. Friedrich, F. Rinaldi, Process modeling of a reversible solid oxide cell (r-SOC) energy storage system utilizing commercially available SOC reactor, Energy Convers. Manage. 142 (2017) 477–493.

[6] C.H. Wendel, Z. Gao, S.A. Barnett, R.J. Braun, Modeling and experimental performance of an intermediate temperature reversible solid oxide cell for high-efficiency, distributed-scale electrical energy storage, J. Power Sourc. 283 (2015) 329–342.

[7] C.H. Wendel, P. Kazempoor, R.J. Braun, Novel electrical energy storage system based on reversible solid oxide cells: system design and operating conditions, J. Power Sourc. 276 (2015) 133–144.

[8] M. Hauck, S. Herrmann, H. Spliethoff, Simulation of a reversible SOFC with Aspen Plus, Int. J. Hydrog. Energy 42 (15) (2017) 10329–10340.

[9] G. Botta, M. Romeo, A. Fernandes, S. Trabucchi, P.V. Aravind, Dynamic modeling of reversible solid oxide cell stack and control strategy development, Energy Convers. Manage. 185 (2019) 636–653.

[10] S. Santhanam, M.P. Heddrich, M. Riedel, K.A. Friedrich, Theoretical and experimental study of reversible solid oxide cell (r-SOC) systems for energy storage, Energy 141 (2017) 202–214.
[11] C.O. Colpan, I. Dincer, F. Hamdullahpur, Thermodynamic modeling of direct internal reforming solid oxide fuel cells operating with syngas, Int. J. Hydrog. Energy 32 (7) (2007) 787–795.
[12] M. Ni, M.K.H. Leung, D.Y.C. Leung, Parametric study of solid oxide fuel cell performance, Energy Convers. Manage. 48 (5) (2007) 1525–1535.
[13] S.H. Chan, C.F. Low, O.L. Ding, Energy and exergy analysis of simple solid-oxide fuel-cell power systems, J. Power Sourc. 103 (2) (2002) 188–200.
[14] A. Monforti Ferrario, F. Santoni, F. Marino, A. Alfano, J. Stenius, M. Noponen, R. Neubauer, V. Cigolotti, Performance evaluation of an anode-supported solid oxide fuel cell short-stack operating with different hydrogen-natural gas blends as stationary combined heat and power system, ECS Meet. Abs. MA2023-01 (54) (2023) 121.
[15] P. Mojaver, A. Chitsaz, M. Sadeghi, S. Khalilarya, Comprehensive comparison of SOFCs with proton-conducting electrolyte and oxygen ion-conducting electrolyte: thermoeconomic analysis and multi-objective optimization, Energy Convers. Manage. 205 (2020) 112455.
[16] U.R. Singh, S. Bhogilla, Exergy analysis of reversible SOFC coupled with organic Rankine cycle and hydrogen storage for renewable energy storage, Int. J. Hydrog. Energy 48 (99) (2023) 39169–39181.
[17] Y. Chen, Y. Luo, Y. Shi, N. Cai, Theoretical modeling of a pressurized tubular reversible solid oxide cell for methane production by co-electrolysis, Appl. Energy 268 (2020) 114927.
[18] C. Bin, Y.S. Hajimolana, V. Venkataraman, M. Ni, P.V. Aravind, Integration of reversible solid oxide cells with methane synthesis (ReSOC-MS) in grid stabilization, Energy Proc. 158 (2019) 2077–2084.
[19] A. Lewandowska-Bernat, U. Desideri, Opportunities of power-to-gas technology in different energy systems architectures, Appl. Energy 228 (2018) 57–67.
[20] L. Wang, J. Düll, F. Maréchal, J. Van herle, Trade-off designs and comparative exergy evaluation of solid-oxide electrolyzer based power-to-methane plants, Int. J. Hydrog. Energy 44 (19) (2019) 9529–9543.
[21] Foit, S.R., I.C. Vinke, L.G.J. de Haart, and R.A. Eichel, Power-to-syngas: an enabling technology for the transition of the energy system? (1521-3773 (Electronic)).
[22] Y. Luo, X.-Y. Wu, Y. Shi, A.F. Ghoniem, N. Cai, Exergy analysis of an integrated solid oxide electrolysis cell-methanation reactor for renewable energy storage, Appl. Energy 215 (2018) 371–383.
[23] L. Zhong, X. Cui, E. Yao, G. Xi, H. Zou, S.H. Jensen, Optimal design and off-design performance improvement for power-to-methane system integrating solid oxide electrolysis cell with methanation reactor, Fuel 356 (2024) 129314.
[24] M. Lototskyy, S. Nyallang Nyamsi, S. Pasupathi, I. Wærnhus, A. Vik, C. Ilea, V. Yartys, A concept of combined cooling, heating and power system utilising solar power and based on reversible solid oxide fuel cell and metal hydrides, Int. J. Hydrog. Energy 43 (40) (2018) 18650–18663.
[25] G. Xiao, A. Sun, H. Liu, M. Ni, H. Xu, Thermal management of reversible solid oxide cells in the dynamic mode switching, Appl. Energy 331 (2023) 120383.
[26] F. Calise, F.L. Cappiello, L. Cimmino, M. Vicidomini, Dynamic simulation modelling of reversible solid oxide fuel cells for energy storage purpose, Energy 260 (2022) 124893.
[27] M. Califano, M. Sorrentino, M.A. Rosen, C. Pianese, Optimal heat and power management of a reversible solid oxide cell based microgrid for effective technoeconomic hydrogen consumption and storage, Appl. Energy 319 (2022) 119268.
[28] E. Reznicek, R.J. Braun, Techno-economic and off-design analysis of stand-alone, distributed-scale reversible solid oxide cell energy storage systems, Energy Convers. Manage. 175 (2018) 263–277.
[29] G. Vialetto, M. Noro, P. Colbertaldo, M. Rokni, Enhancement of energy generation efficiency in industrial facilities by SOFC – SOEC systems with additional hydrogen production, Int. J. Hydrog. Energy 44 (19) (2019) 9608–9620.
[30] R.K. Akikur, R. Saidur, H.W. Ping, K.R. Ullah, Performance analysis of a co-generation system using solar energy and SOFC technology, Energy Convers. Manage. 79 (2014) 415–430.
[31] M. Rokni, Analysis of a polygeneration plant based on solar energy, dual mode solid oxide cells and desalination, Int. J. Hydrog. Energy 44 (35) (2019) 19224–19243.
[32] N.C. Ullvius, M. Rokni, A study on a polygeneration plant based on solar power and solid oxide cells, Int. J. Hydrog. Energy 44 (35) (2019) 19206–19223.
[33] G. Buffo, D. Ferrero, M. Santarelli, A. Lanzini, Energy and environmental analysis of a flexible Power-to-X plant based on reversible solid oxide cells (rSOCs) for an urban district, J. Energy Stor. 29 (2020) 101314.
[34] Z. Aghaziarati, M. Ameri, M. Bidi, A year-round investigation of an integrated system based on reversible solid oxide cell, Energy Convers. Manage. 311 (2024) 118553.
[35] Z. Aghaziarati, M. Ameri, M. Bidi, Exergy based yearly performance analysis of a poly-generation system for a small-town application, Renew. Energy 237 (2024) 121604.
[36] P. Mojaver, M. Abbasalizadeh, S. Khalilarya, A. Chitsaz, Co-generation of electricity and heating using a SOFC-ScCO2 Brayton cycle-ORC integrated plant: investigation and multi-objective optimization, Int. J. Hydrog. Energy 45 (51) (2020) 27713–27729.
[37] D. Villareal Singer, Reversible solid oxide cells for bidirectional energy conversion in spot electricity and fuel markets. https://doi.org/10.7916/D8V988P6.
[38] M.F. Ezzat, I. Dincer, Energy and exergy analyses of a novel ammonia combined power plant operating with gas turbine and solid oxide fuel cell systems, Energy 194 (2020) 116750.
[39] C. Wang, M. Chen, M. Liu, J. Yan, Dynamic modeling and parameter analysis study on reversible solid oxide cells during mode switching transient processes, Appl. Energy 263 (2020) 114601.
[40] Z. Aghaziarati, A.H. Aghdam, Thermoeconomic analysis of a novel combined cooling, heating and power system based on solar organic Rankine cycle and cascade refrigeration cycle, Renew. Energy 164 (2021) 1267–1283.
[41] B. Patel, N.B. Desai, S.S. Kachhwaha, Thermo-economic analysis of solar-biomass organic Rankine cycle powered cascaded vapor compression-absorption system, Solar Energy 157 (2017) 920–933.
[42] L.T. Scarabelot, C.R. Rambo, G.A. Rampinelli, A relative power-based adaptive hybrid model for DC/AC average inverter efficiency of photovoltaics systems, Renew. Sustain. Energy Rev. 92 (2018) 470–477.
[43] J. Sanz-Bermejo, J. Muñoz-Antón, J. Gonzalez-Aguilar, M. Romero, Part load operation of a solid oxide electrolysis system for integration with renewable energy sources, Int. J. Hydrog. Energy 40 (26) (2015) 8291–8303.
[44] M. Chaczykowski, Transient flow in natural gas pipeline – the effect of pipeline thermal model, Appl. Math. Model. 34 (4) (2010) 1051–1067.
[45] https://re.jrc.ec.europa.eu/pvg_tools/en/.
[46] C. Janke, M.S. Duyar, M. Hoskins, R. Farrauto, Catalytic and adsorption studies for the hydrogenation of CO2 to methane, Appl. Catal. B: Environ. 152-153 (2014) 184–191.
[47] M. Netusil, P. Ditl, Comparison of three methods for natural gas dehydration, J. Nat. Gas Chem. 20 (5) (2011) 471–476.
[48] E. Riensche, J. Meusinger, U. Stimming, G. Unverzagt, Optimization of a 200 kW SOFC cogeneration power plant. Part II: variation of the flowsheet, J. Power Sourc. 71 (1) (1998) 306–314.
[49] R.J. Braun, S.A. Klein, D.T. Reindl, Evaluation of system configurations for solid oxide fuel cell-based micro-combined heat and power generators in residential applications, J. Power Sourc. 158 (2) (2006) 1290–1305.
[50] R.J. Braun, Optimal Design and Operation of Solid Oxide Fuel Cell Systems for Small-scale Stationary Applications, University of Wisconsin, MADISON, 2002.
[51] S.L. Ebbehoj, Integration of CO2 Air Capture and Solid Oxide Electrolysis for Methane Production, Denmark Technical University, 2015.
[52] A. Perna, M. Minutillo, E. Jannelli, Designing and analyzing an electric energy storage system based on reversible solid oxide cells, Energy Convers. Manage. 159 (2018) 381–395.
[53] L. Khani, S.M.S. Mahmoudi, A. Chitsaz, M.A. Rosen, Energy and exergoeconomic evaluation of a new power/cooling cogeneration system based on a solid oxide fuel cell, Energy 94 (2016) 64–77.
[54] F.A. Al-Sulaiman, I. Dincer, F. Hamdullahpur, Energy analysis of a trigeneration plant based on solid oxide fuel cell and organic Rankine cycle, Int. J. Hydrog. Energy 35 (10) (2010) 5104–5113.
[55] F. Lonis, V. Tola, G. Cau, Renewable methanol production and use through reversible solid oxide cells and recycled CO2 hydrogenation, Fuel 246 (2019) 500–515.
[56] J. Alsarraf, A.A. Alnaqi, A.A.A.A. Al-Rashed, Thermodynamic modeling and exergy investigation of a hydrogen-based integrated system consisting of SOFC and CO2 capture option, Int. J. Hydrog. Energy 47 (62) (2022) 26654–26664.
[57] Y. Cao, T. parikhani, A solar-driven lumped SOFC/SOEC system for electricity and hydrogen production: 3E analyses and a comparison of different multi-objective optimization algorithms, J. Clean. Prod. 271 (2020) 122457.
[58] M. Ni, 2D thermal modeling of a solid oxide electrolyzer cell (SOEC) for syngas production by H2O/CO2 co-electrolysis, Int. J. Hydrog. Energy 37 (8) (2012) 6389–6399.
[59] C.H. Wendel, P. Kazempoor, R.J. Braun, A thermodynamic approach for selecting operating conditions in the design of reversible solid oxide cell energy systems, J. Power Sourc. 301 (2016) 93–104.
[60] S.H. Jensen, P.H. Larsen, M. Mogensen, Hydrogen and synthetic fuel production from renewable energy sources, Int. J. Hydrog. Energy 32 (15) (2007) 3253–3257.
[61] F. Marino, A. Monforti Ferrario, F. Santoni, A. Alfano, M. Noponen, R. Neubauer, V. Cigolotti, E. Jannelli, Performance evaluation of an anode-supported SOFC short-stack operating with different fuel blends as stationary-CHP system, J. Electrochem. Soc. 171 (5) (2024) 054511.

[62] P. Mojaver, S. Khalilarya, A. Chitsaz, M. Assadi, Multi-objective optimization of a power generation system based SOFC using Taguchi/AHP/TOPSIS triple method, Sustain. Energy Technol. Assess. 38 (2020) 100674.
[63] P. Mojaver, S. Khalilarya, A. Chitsaz, Multi-objective optimization and decision analysis of a system based on biomass fueled SOFC using couple method of entropy/VIKOR, Energy Convers. Manage. 203 (2020) 112260.
[64] P. Marocco, D. Ferrero, A. Lanzini, M. Santarelli, Benefits from heat pipe integration in H2/H2O fed SOFC systems, Appl. Energy 241 (2019) 472–482.
[65] L. Jianbo, L. Kai, H. Xiaolong, Z. Chen, C. Fulin, K. Xiangqiang, A novel absorption–compression combined refrigeration cycle activated by engine waste heat, Energy Convers. Manage. 205 (2020) 112420.
[66] K. Salhi, M. Korichi, K.M. Ramadan, Thermodynamic and thermo-economic analysis of compression–absorption cascade refrigeration system using low-GWP HFO refrigerant powered by geothermal energy, Int. J. Refrig. 94 (2018) 214–229.
[67] S. Yu, D. Hong, Y. Lee, S. Lee, K. Ahn, Development of a catalytic combustor for a stationary fuel cell power generation system, Renew. Energy 35 (5) (2010) 1083–1090.
[68] J. Gao, Y. Wang, Y. Ping, D. Hu, G. Xu, F. Gu, F. Su, A thermodynamic analysis of methanation reactions of carbon oxides for the production of synthetic natural gas, RSC Adv. 2 (6) (2012) 2358–2368.
[69] J. Kopyscinski, T. Schildhauer, S. Biollaz, Production of synthetic natural gas (SNG) from coal and dry biomass – a technology review from 1950 to 2009, Fuel 89 (2010) 1763–1783.
[70] M. Tommasi, S.N. Degerli, G. Ramis, I. Rossetti, Advancements in CO2 methanation: a comprehensive review of catalysis, reactor design and process optimization, Chem. Eng. Res. Des. 201 (2024) 457–482.